

NGC 5266: AN ELLIPTICAL GALAXY WITH A DUST RING¹

S. R. VARNAS
 Monash University

F. BERTOLA
 Institute of Astronomy, University of Padova

G. GALLETTA
 Padova Astronomical Observatory

AND

K. C. FREEMAN AND D. CARTER
 Mount Stromlo and Siding Spring Observatories, Institute of Advanced Studies, Australian National University

Received 1985 November 25; accepted 1986 July 25

ABSTRACT

Results of an inquiry into the nature of the southern galaxy NGC 5266 are presented. This object has been classified as an S0 in the Second Reference Catalog. Our surface photometry indicates that it is rather an E4 class elliptical with a narrow and slightly warped dust ring wrapping its stellar body in the plane containing its short axis. The extensive spectroscopic observations reveal a very fast cylindrical rotation of the stellar component ($V_{\max} = 212 \pm 7 \text{ km s}^{-1}$) around the short axis and smaller rotation ($V = 43 \pm 16 \text{ km s}^{-1}$) around the long axis. The stellar velocity dispersion is $210 \pm 6 \text{ km s}^{-1}$ in the center and decreases with radius down to as low as 100 km s^{-1} at around $R = 20''$. The gas associated with dust rotates around the major axis of the galaxy with a velocity of $260 \pm 10 \text{ km s}^{-1}$. In the warp the gas motions are prograde with respect to the major axis stellar rotation. Radio observations of the 21 cm line in emission indicate a large amount of H I gas [$M_{\text{HI}} = 1.75 \times 10^{10} (H/50)^{-2} M_{\odot}$], probably distributed in a rotating disk. Analysis of the kinematical data should lead us to the conclusion that the true shape of the stellar component in this galaxy is probably triaxial (nearly oblate). Dynamical modeling of the dissipative evolution of gas disks embedded in triaxial potentials shows that the observed morphology of the dust is unlikely to be produced by an incomplete settling of the gas disk to the preferred plane in a stationary potential. We also find that a quasi-settled warped disk in a figure which is slowly tumbling about the short axis, retrograde to the observed streaming motions, fits the observations very well.

Subject headings: galaxies: individual — galaxies: internal motions — galaxies: photometry — galaxies: structure — interstellar: matter

I. INTRODUCTION

A class of galaxies characterized by an elliptical-like body and a disk or a ring of gas and dust with no substantial population of stars in it, whose existence has been pointed out by Bertola and Galletta (1978), has attracted considerable attention in recent years. These objects are interesting in several aspects. First, their stellar and gaseous components are quite distinct dynamically, which poses questions about the origin of gas (see, for example, Graham 1979). Second, the orientation of the dust lane together with the kinematics of the stellar and the gaseous components can shed some light on the three-dimensional shape of the potential in which the gas is embedded (Tohline, Simonson, and Caldwell 1982). Third, the fact that many of these objects are strong radio sources (Kotanyi and Ekers 1979) suggests some interesting ideas about the mechanism for the fueling of the radio sources in general (Gunn 1979). A systematic search for objects of similar morphology (Hawarden *et al.* 1981; Ebneter and Balick 1985) revealed ~ 100 galaxies possibly belonging to this class. A more detailed study of the individual objects of this type (Graham 1979; Sharples *et al.* 1983; Möllenhoff 1982; Caldwell

1984; Bertola, Galletta, and Zeilinger 1985; Möllenhoff and Marenbach 1986) and of possibly related systems (spindle galaxies; see Schechter and Gunn 1978; Schweizer 1980; Schweizer, Whitmore, and Rubin 1983; Schechter *et al.* 1984; Knapp, van Driel, and van Woerden 1985) has also been undertaken. Of particular interest are those galaxies whose minor-axis dust lanes are warped. Their kinematical study can reveal whether the motion of the stellar component is prograde or retrograde with respect to the gas motion in the warps, a fact which may be related to the interpretation of the warps as stationary or transient phenomena (Bertola, Galletta, and Zeilinger 1985). In the galaxy studied in this paper, NGC 5266, prograde motions have been found by Caldwell (1984). In addition to the presentation of new and more extended observational data, we make a theoretical study of the two above possibilities, showing that a triaxial model of NGC 5266, slowly tumbling in a retrograde direction with respect to the observed stellar streaming, can produce a warped disk in a quasi-settled configuration, while the transient warps due to incomplete settling in a stationary potential proposed by Caldwell (1984) fail to materialize.

II. SURFACE PHOTOMETRY

A photograph of NGC 5266 was obtained at the prime focus of the AAT in 1980 July, using IIIa-J emulsion, GG 385 filter, and the triplet corrector. The exposure time was 40 minutes.

¹ Partially based on observations collected at the European Southern Observatory, La Silla, Chile.

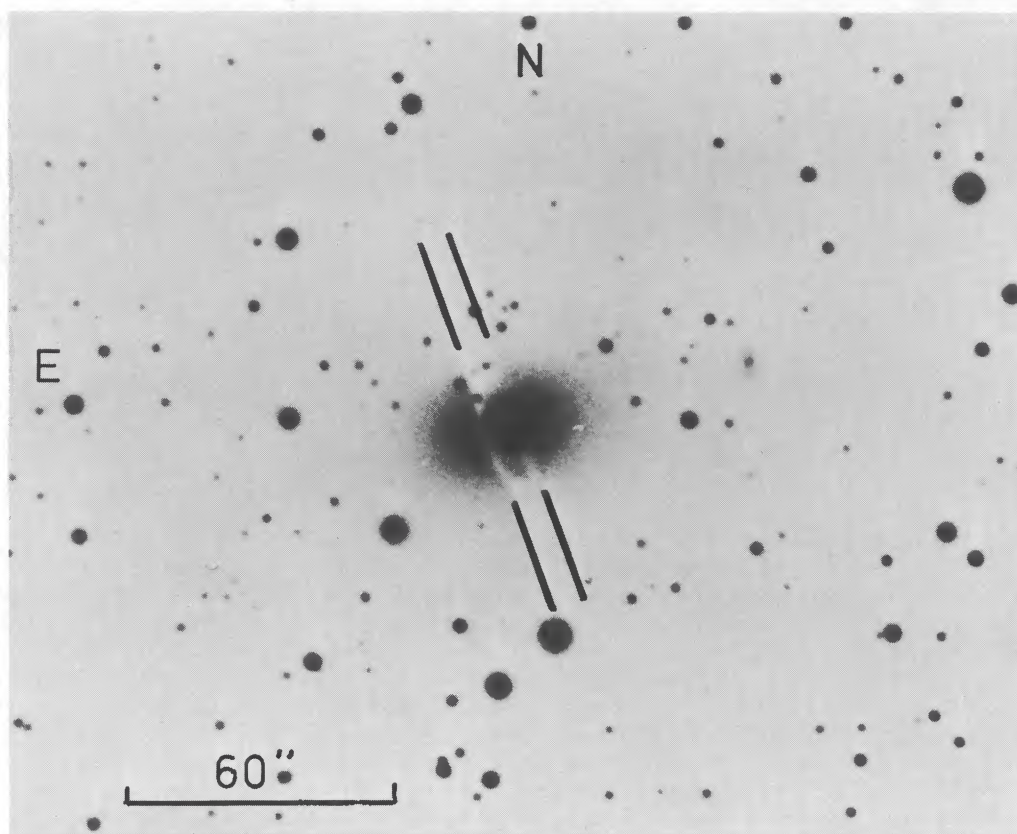


FIG. 1.—AAT prime focus plate of NGC 5266 treated with unsharp masking. The two positions of the slit corresponding to the “foreground” and the “background” are shown.

The photograph presented in Figure 1 was processed by unsharp masking (Malin 1979) to bring out the fine details.

Conventional surface photometry techniques were applied to PDS scans of the original photograph. The surface brightness profile along both major and minor axes is shown in the top graph of Figure 2. We can see that the data points fit the de Vaucouleurs (1984) empirical law (*straight lines*)

$$\mu = \mu_e + 8.33[(r/r_e)^{1/4} - 1] \quad (1)$$

very well, except for the small area along the major axis in the east-southeast, where the dust lane is (*dashed line*). The parameters of the best fit are $\mu_e = 23.80$ and $r_e = 65''$. Fitting ellipses to the isophotes gave us the relationship between the radius and the ellipticity $\epsilon = (1 - b/a)$ as well as the position angle (P.A.) of the major axis of the ellipse (Fig. 2). Apart from the two innermost points, the fits show that the isophotes are closely concentric similar ellipses with $\epsilon = 0.37 \pm 0.03$, and the P.A. of the major axis $110^\circ \pm 3^\circ$.

Images of NGC 5266 in five wavebands (*UBVRI*) have been obtained with the RGO/RCA CCD on the AAT as part of a large survey of radio and nonradio ellipticals (Carter, Jenkins and Sadler 1986). The structure of the stellar component is best seen in the *I*-band image, where the absorption due to dust is least. The ellipse-fitting to the isophotes produced values of ϵ decreasing from 0.38 ± 0.01 at $10''$ radius to 0.34 ± 0.01 at $40''$ radius and a constant P.A. of the major axis at $107^\circ \pm 1^\circ$. The surface brightness profile in this waveband was also well represented by de Vaucouleurs' law with $r_e = 75'' \pm 10''$. These results agree well with our photographic photometry.

In the photographic image of the galaxy (Fig. 1) there is a hint of the warp in the north-northeast end of the dust lane. To

see the full extent of this warp we took the CCD *B* image (Fig. 3a) and subtracted the $r^{1/4}$ fit to its surface brightness (Fig. 3b). The resultant image shows the warp in the dust lane in the north-northeast clearly. Its presence is also confirmed by a *B-I* image (Fig. 3c). Here red colors are represented by bright regions, which are good tracers of the dust. We notice that in addition to the warped dust ring, there is also a red patch in the area of the nucleus.

III. SLIT SPECTROSCOPY

a) Observations

The observations at four P.A.'s (17° , 62° , 107° , and 152°) were made with the AAT on several nights in 1980 April and May. The RGO spectrograph was used, with the IPCS as detector. The wavelength range was $4800\text{--}5800 \text{ \AA}$ at a dispersion of 33 \AA mm^{-1} ($0.50 \text{ \AA pixel}^{-1}$). The slit width was $2''.7$, which projects to 2.1 \AA at the detector. Perpendicular to the dispersion, 1 pixel is $2''.3$. The cumulative exposure times for each position angle are listed in Table 1. Table 2 gives details of the observed standard stars.

TABLE 1
GALAXY OBSERVATIONS WITH
THE AAT

| Position Angle | Exposure (s) |
|-------------------|--------------|
| 107° | 9000 |
| 152° | 6000 |
| 62° | 6600 |
| 17° | 6000 |

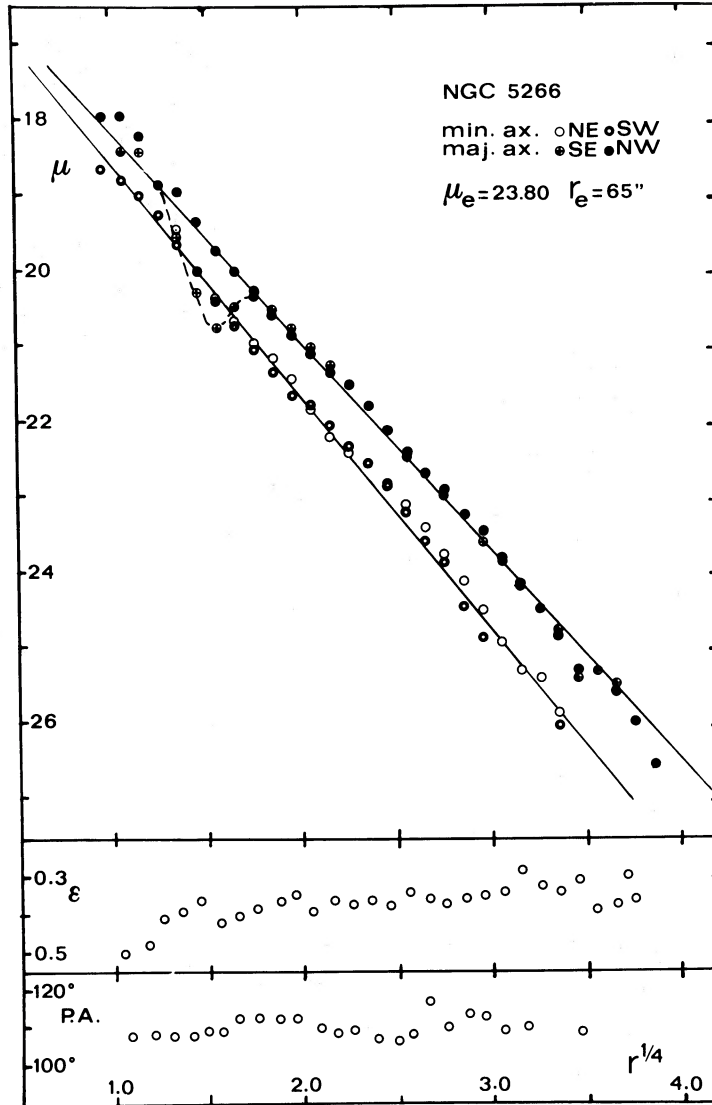


FIG. 2.—Properties of surface brightness distribution from the AAT plate (IIIa-J + GG 385): the fit to the de Vaucouleurs law (*top*), eccentricity (*middle*), and P.A. of the major axis of the isophotes vs. $r^{1/4}$ (r in arcsec).

More spectra were taken with the ESO 1.5 m telescope in 1982 March (P.A. 112° and 32°) and 3.6 m reflector in 1983 February (P.A. 21°). The Boller and Chivens spectrograph with the image tube was used in the 3500–4500 Å wavelength region. The dispersion was 39 \AA mm^{-1} , exposure time was 90 minutes in each case, while the scale perpendicular to the dispersion was $87'' \text{ mm}^{-1}$ for the 1.5 m and $38.5'' \text{ mm}^{-1}$ for the 3.6 m spectra. Two exposures were taken at P.A. 21° , corresponding to the foreground and background of the dust ring (see Fig. 1).

TABLE 2
STANDARD STAR OBSERVATIONS

| Object | Spectral Class | Magnitude | Exposure (s) |
|-----------------|----------------|-----------|--------------|
| HD 88293 | G8 III | 8.9 | 400 |
| HD 88226 | K0 III | 8.6 | 300 |
| HD 110253 | K2 III | 8.2 | 300 |

b) Reduction

Standard procedures were followed to prepare the spectroscopic IPCS data for the analysis. The instrumental response was found by measuring the flat field before each night and the twilight sky in early morning. To remove the pixel-to-pixel quantum efficiency variations and the vignetting effects, all the spectra measured during the night were divided by the night's flat field and the twilight sky profile along the slit. Wavelength calibration and removal of geometrical distortions were performed using comparison spectra of the AAT argon arc. About 30 lines have been identified in a region between 4933 Å and 5682 Å, and a third-order polynomial has been fitted to the dispersion relationship. The fits were excellent, with the standard deviation 0.2–0.3 pixel ($5\text{--}8 \text{ km s}^{-1}$) or less for most of the spectra and never exceeding 0.5. The coefficients so obtained were used to rebin our data from raw pixels to a $\log \lambda$ scale, producing spectra with uniform shifts. About 20–30 rows containing sky measurements were averaged and the average was subtracted from each frame. The strongest sky feature at 5577

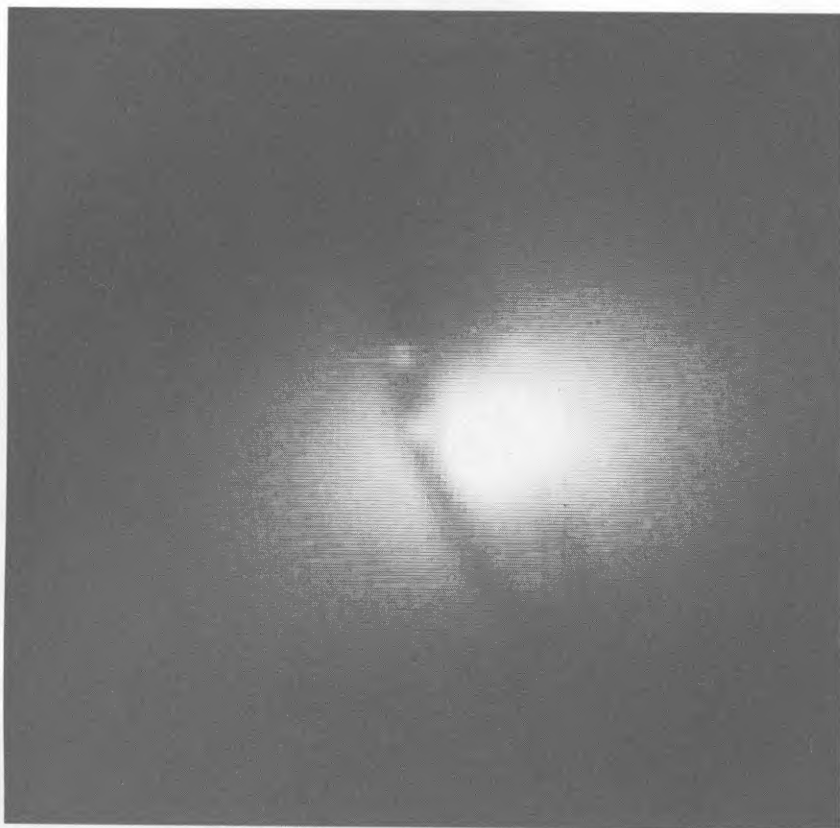


FIG. 3a

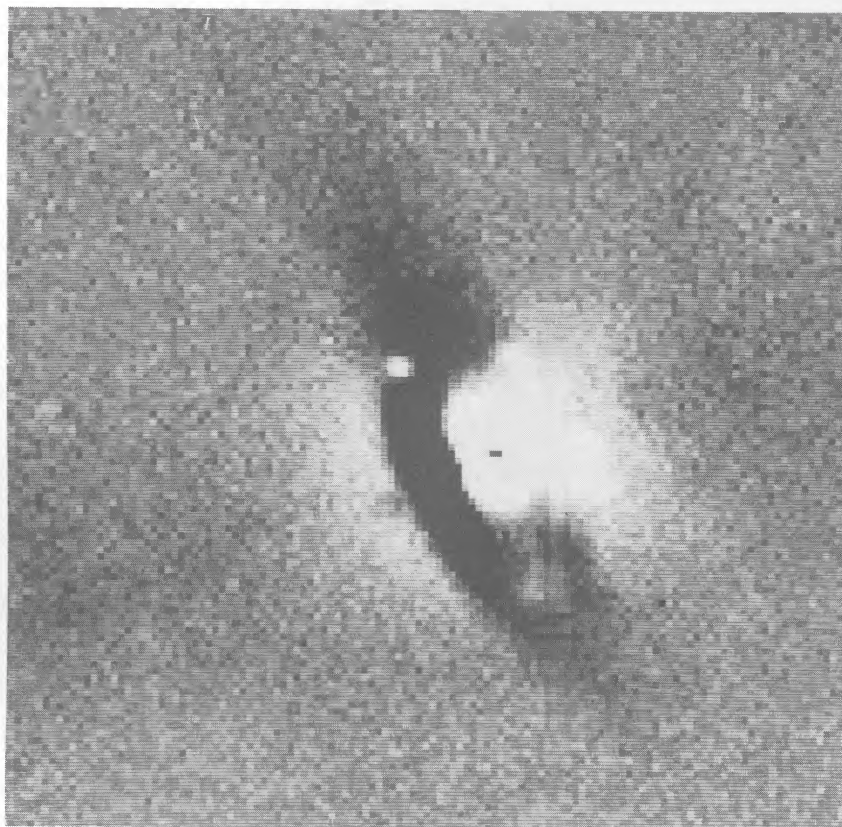


FIG. 3b

FIG. 3.—CCD images of NGC 5266. Size of frame is $62''.72$. (a) *B* image, (b) *B* image with $r^{1/4}$ law subtracted, (c) *B-I* image.

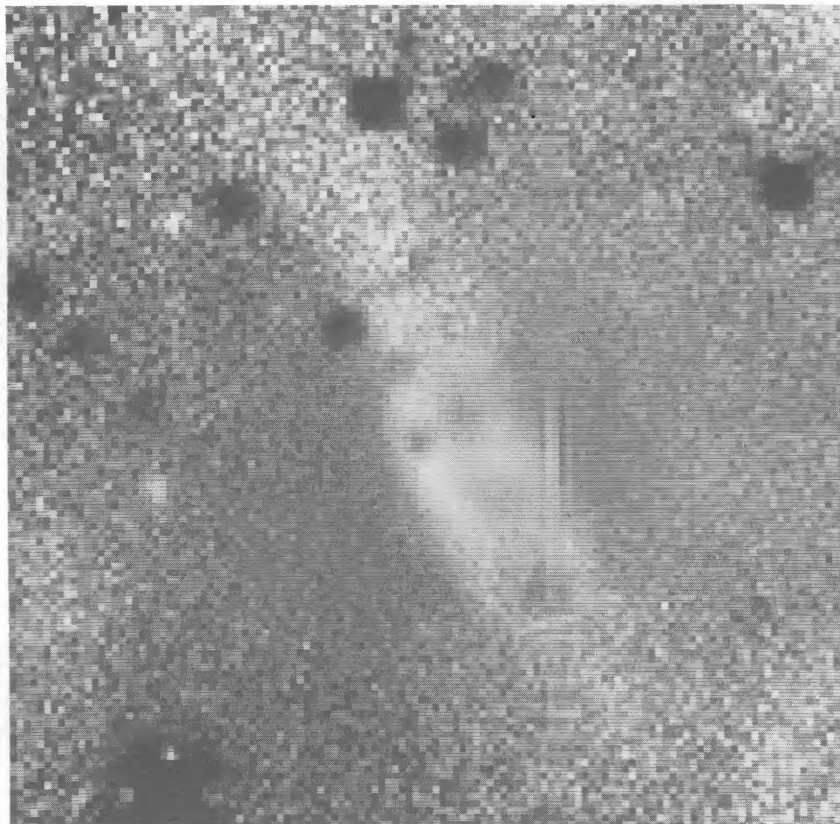


FIG. 3c

\AA was not totally removed by this procedure, and we had to interpolate linearly across it. We also checked whether the center of the galaxy is in the same row number for all exposures of the particular position angle and applied the relevant shift if necessary. Finally, we added all exposures taken at the same position angle and thus obtained four two-dimensional frames with reduced galaxy spectra corresponding to each position angle. The spectra of the three standard stars (K giants) observed were also prepared in a similar manner. The sum of all three standard stars was used as a template for the cross-correlation with the galaxy spectra in most of the cases. Evaluating the rotation curve along the minor axis, we also used each of the standards separately as templates to check the effect of the mismatch between the template and galaxy spectra (see § III d.) Visual comparisons were also made and showed a very good match: of ~ 30 features identified in each spectrum, only two or three minor lines did not have their counterparts in the other spectrum.

To remove the low-frequency variations, we divided all our spectra by a seventh order polynomial fitted to the continuum. This relatively high order polynomial was needed to follow the variations of the continuum, which were weakly affected by the residual S-distortion of the detector. Dividing by this seventh-order polynomial does not affect the strengths or shapes of any of the absorption lines in our spectral region. The mean intensities of the spectra were then set to zero, and 10% of the spectra were masked at each end by multiplication by a cosine bell. This reduces the leakage, due to the finite length of our measurements, in the subsequent Fourier analysis. A similar procedure, including wavelength and intensity calibrations, continuum flattening, and end-masking, was applied to the

ESO spectra. The emission lines present in these plates were measured using the Grant machine at the ESO headquarters in Garching, while for the absorption lines PDS scans of the plates were used.

c) Analysis

The processed spectra were then analyzed to produce velocities and velocity dispersions. The Fourier quotient method described by Sargent *et al.* (1977) was used to find the shifts and broadenings of the absorption lines. Although this method has been extensively tested by many workers and shown to be quite reliable, we also in some cases applied the cross correlation technique of Tonry and Davis (1979) for the velocity determination, as a measure of consistency. The spectra were filtered in the wavenumber domain before cross-correlating. The filter was designed to remove remains of the continuum variation left after flattening the spectra, as well as the high-frequency photon noise, which does not carry any useful information about phase shifts. The bandpass filter starts at wavenumber $k = 10$, rises linearly to the value of 1 at $k = 20$, then has a cosine bell shape at the end, starting to roll off at $k = 200$ and reaching zero at $k = 250$. In the Fourier quotient program we fitted the quotients in the wavenumber range $10 < k < 250$, which is consistent with the window used in the cross-correlation program. From the rotation curves presented in Fig 4 we can see that the two methods are in excellent agreement. The error bars shown are the formal errors of the cross-correlation technique, unless stated otherwise.

In the IPCS data, we have also seen one emission line, $[\text{O III}] \lambda 5007$, in the observed spectral region. It was strong enough to obtain velocities of the ionized gas projected along

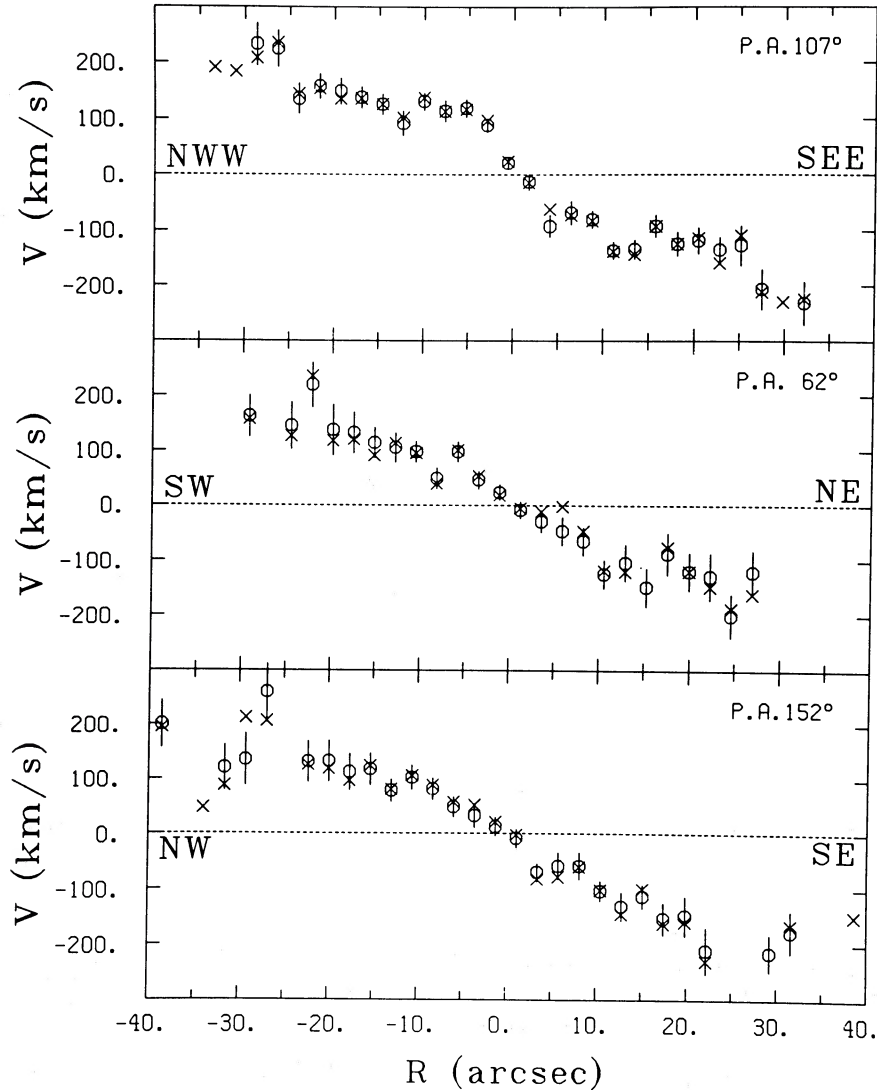


FIG. 4.—The three rotation curves derived from the absorption spectra taken with the slit at P.A. 107° , 62° , and 152° . Crosses, velocities obtained by the Fourier quotient method; circles with error bars, result of the cross-correlation analysis.

the line of sight. That was done by fitting the Gaussian profiles to the emission lines. Some of the spectra with poor signal-to-noise ratio have been smoothed with a running three-point mean.

Spectra taken in the other spectral region revealed strong $[\text{O II}] \lambda 3727$ doublet emission. In many cases it was resolved, and consequently we have been able to measure gas velocities using each component separately as well as the wings of the feature. Those values were then averaged.

d) Results

Rotation curves of the elliptical-like stellar component of NGC 5266 are shown in Figures 4–6. The central redshift was found to be $V_0 = 3044 \text{ km s}^{-1}$ and was subtracted. No correction for the heliocentric velocity of the standard stars was applied, because it was found to be insignificant (less than 10 km s^{-1}). The top graph of Figure 4 represents stellar velocities along the apparent major axis (P.A. = 107°). From this figure it is immediately obvious that NGC 5266 has a very high rotation along the major axis. Its rotation curve rises linearly from

the center until it reaches a plateau somewhere around $|R| = 5''\text{--}10''$, with the average velocity around 100 km s^{-1} . In this rather flat region the rotation curve still has a tendency to rise, and it reaches $\sim 140 \text{ km s}^{-1}$ at $|R| = 25''$. The average value derived from eight measurements centered around $|R| = 21''$ is $137 \pm 6 \text{ km s}^{-1}$, in exact agreement with the half-width of the stellar velocity amplitude found by Caldwell (1984) at P.A. = 114° . Then there is a sudden jump in velocity beyond $R = 25''$ with $V_{\text{max}} = 212 \pm 7 \text{ km s}^{-1}$. (The error estimates quoted here are the standard errors of the mean.) The fact that this jump occurs for three or four points on each side convinces us that it is a real feature of the object. Möllenhoff and Marenbach (1986) have noticed a similar rise of velocity in the SEE part of the major axis in this galaxy. Such a high velocity makes NGC 5266 the fastest rotating elliptical of which we are aware (see Table 3 of Davies *et al.* 1983 for the compilation of data on the kinematics of elliptical galaxies). From the other two rotation curves in this figure, measured with the slit at $\pm 45^\circ$ from the major axis, we can deduce the dependence of the rotation on the Z-coordinate (parallel to the

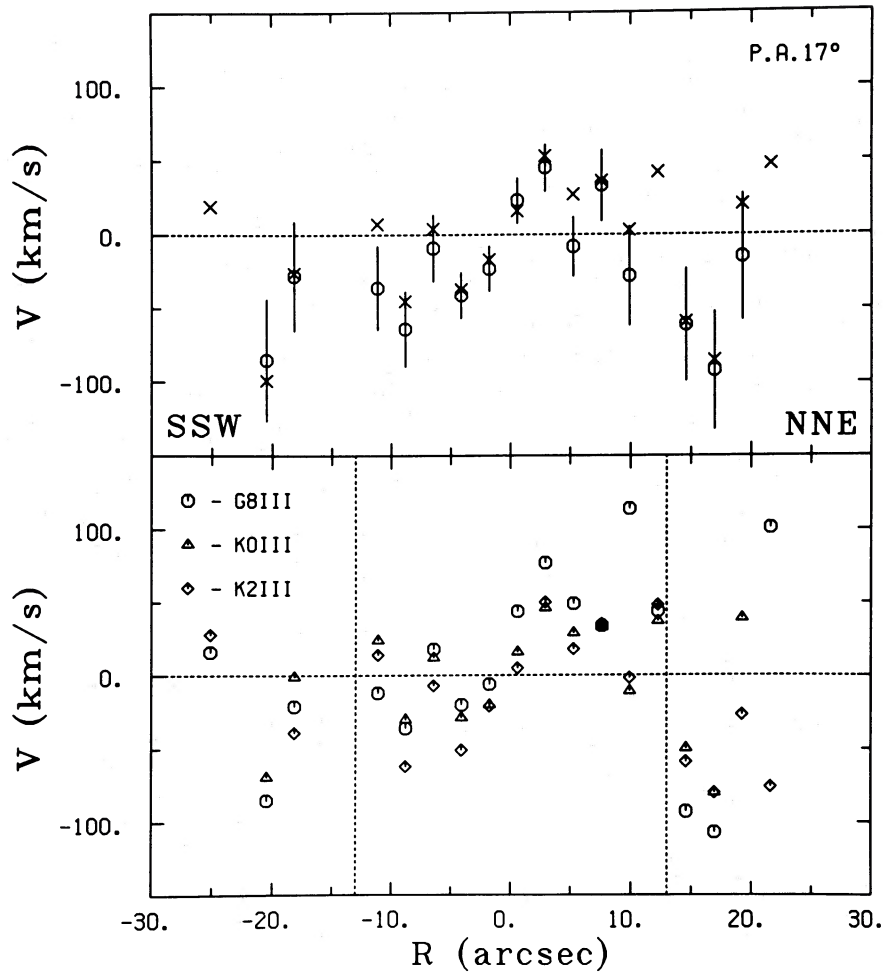


FIG. 5.—Minor axis (P.A. = 17°) rotation curve derived from the absorption spectra. (top) Composite template was used, conventions same as in Fig. 4. (bottom) Fourier quotient method was used for each of the three templates separately. Vertical dashed lines limit the region where the nonzero minor axis rotation is evident.

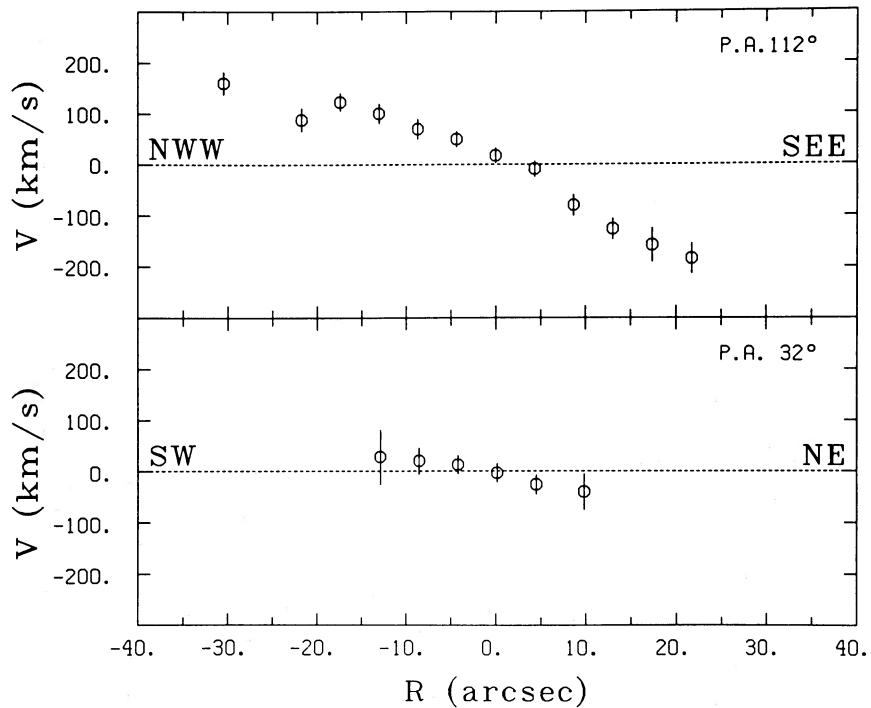


FIG. 6.—The two stellar rotation curves at P.A. = 112° and 32° obtained at ESO, using the Fourier quotient method

TABLE 3
DEPENDENCE OF ROTATIONAL VELOCITY
(km s^{-1}) ON HEIGHT Z

| Z (1) | V_- (2) | V_+ (3) | V_{rot} (4) |
|------------|--------------|--------------|-------------------------|
| $R = 7''$ | | | |
| -7..... | 103 | 121 | 112 |
| 0..... | 117 | 103 | 110 |
| +7..... | 97 | 97 | 97 |
| $R = 14''$ | | | |
| -14..... | 126 | 120 | 123 |
| 0..... | 120 | 124 | 122 |
| +14..... | 129 | 153 | 141 |

apparent minor axis and pointing northeast). We measured velocities at two distances from the rotation axis, $7''$ and $14''$, and three heights, $-7''$, $0''$, $7''$ and $-14''$, $0''$, $14''$ respectively. Results are shown in Table 3; V_- represents velocities on the eastern end ($< V_0$) and V_+ those on the western end ($> V_0$). The averaged rotational velocities V_{rot} are shown in column (4). With the average error bars of each measurement being $20\text{--}40 \text{ km s}^{-1}$, we can see that the rotational velocity of the stellar component in this galaxy is constant with Z up to $|Z| = 14''$ within the measurement errors. That suggests to us that this galaxy belongs to the class of cylindrical rotators, which have the same amount of rotation for all values of Z , as in the case of NGC 5128 (Bertola, Galletta, and Zeilinger 1985; Wilkinson *et al.* 1986).

Figure 5 illustrates the rotation curve along the minor axis

of the galaxy (P.A. = 17°), which happens to coincide with the orientation of the dust lane. Careful examination of the behavior of this rotation curve, particularly its inner part within $R = \pm 13''$, reveals what appears to be nonzero rotation along this axis. Velocities shown on the top graph were obtained using Fourier quotient and cross-correlation procedures with a composite template, as were all the velocities in Figure 4. On the lower graph we show velocities obtained using the Fourier quotient method and taking each standard as a template separately. The scatter of the points gives us some indication of the possible errors in the rotation curve due to the mismatch of the template and galaxy spectra. Although the scatter is significant, the same trend revealed in the top curve persists: north-northeast recedes from us faster than south-southwest. We have estimated the average maximum rotation velocity along the minor axis as $43 \pm 16 \text{ km s}^{-1}$ (the internal error is quoted here). A few more comments about this rotation curve are in order. Since the slit was positioned near the inner edge of the dust ring, the light from the central few rows is integrated through the entire stellar body. However, in the outer regions of the slit, the obscuration by dust probably restricted us to measuring the velocities of stars only in the front of the stellar body. It may also be possible that some absorption spectra in these regions are dominated by a stellar component in the disk. This may be the reason for the seeming reversal of the rotation curve in the north-northeast of Figure 5, where the larger concentration of dust is apparent. The rotation curves derived at ESO are shown in Figure 6 (P.A. = 112° and 32°) and confirm the large rotation derived from the IPCS spectra.

We used all these stellar rotation curves to locate the kinematic axis of NGC 5266. The averaged velocity gradients were computed and plotted as a function of P.A. (Figure 7). The

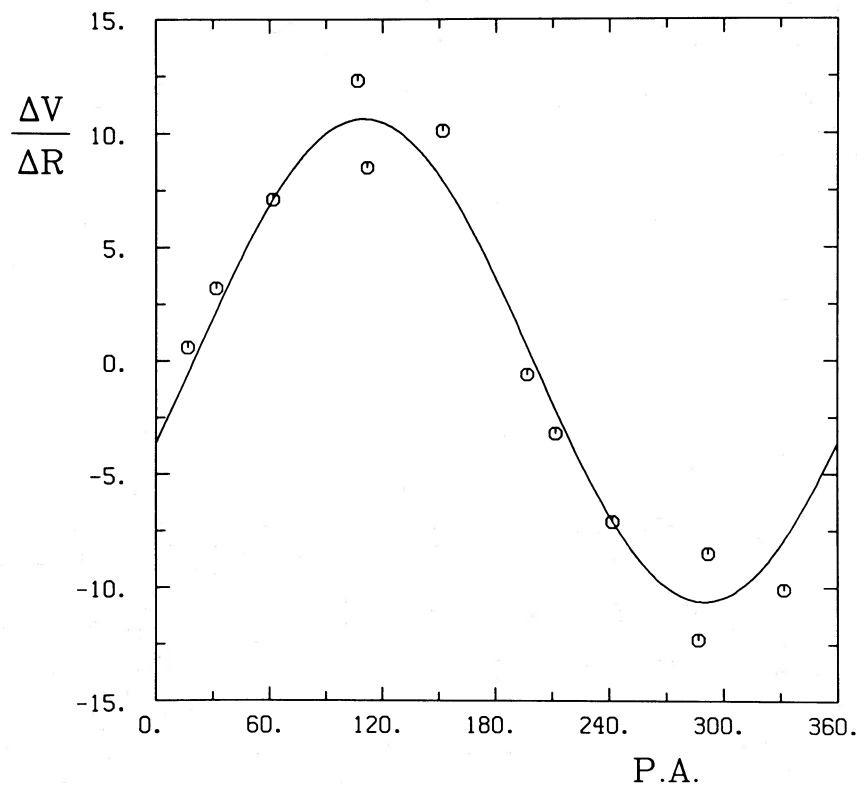


FIG. 7.—Fit of sinusoid to velocity gradient variation with P.A.

sinusoid fitted to the data points gave us the P.A. of the kinematic line of nodes as 110° .

Figures 8 and 9 show the projected line-of-sight velocities of the gas in NGC 5266 determined from the measurements of [O III] and [O II] emission lines respectively. The top curve of Figure 8 represents velocities along the apparent minor axis. This is the approximate orientation of the major axis of the gas ring, so we have been able to detect emission over a fairly large interval of radii, particularly in the south-southwest. Here the radial velocity rises up to 230 km s^{-1} at $R = -17''$. It is important to note that the gas is rotating in the opposite direction to the stars along the minor axis, which strongly suggests its external origin. The two rotation curves measured at $\pm 45^\circ$ angles to the dust lane show significant amounts of emission far away from it, particularly in the northeast (P.A. = 62°). Gas velocities at a P.A. of 21° are displayed in Figure 9. The top rotation curve corresponds to the "foreground" of the dust lane, while the bottom one reveals rotation in the "background" part of it. The slit positions are shown on the

photograph in Figure 1. The extent of the latter in the north-northeast is larger and shows rotational velocities up to 250 km s^{-1} at $R \approx 23''$. It was noticed here that the central redshift for the gas in the foreground was 50 km s^{-1} lower than that in the background and that of the stars. However, it is not clear whether this effect is real, because velocities obtained from [O III] emission in the foreground (P.A. = 17°) do not show the central redshift significantly lower than the stellar one ($\Delta V < 15 \text{ km s}^{-1}$).

To get better spatial coverage of gas velocities, we attempted to observe this galaxy in the [O III] $\lambda 5007$ line with the imaging Fabry-Perot interferometer Taurus (Atherton *et al.* 1982) on the AAT. Because of the dominant contribution of the stellar component and the weakness of the emission lines, the signal-to-noise ratio was very poor, and it was not possible to measure gas velocities with any confidence, but the results have been used to compare the gas distribution with the morphology provided by the model described in § VII of this paper.

Stellar velocity dispersion profiles for the four position

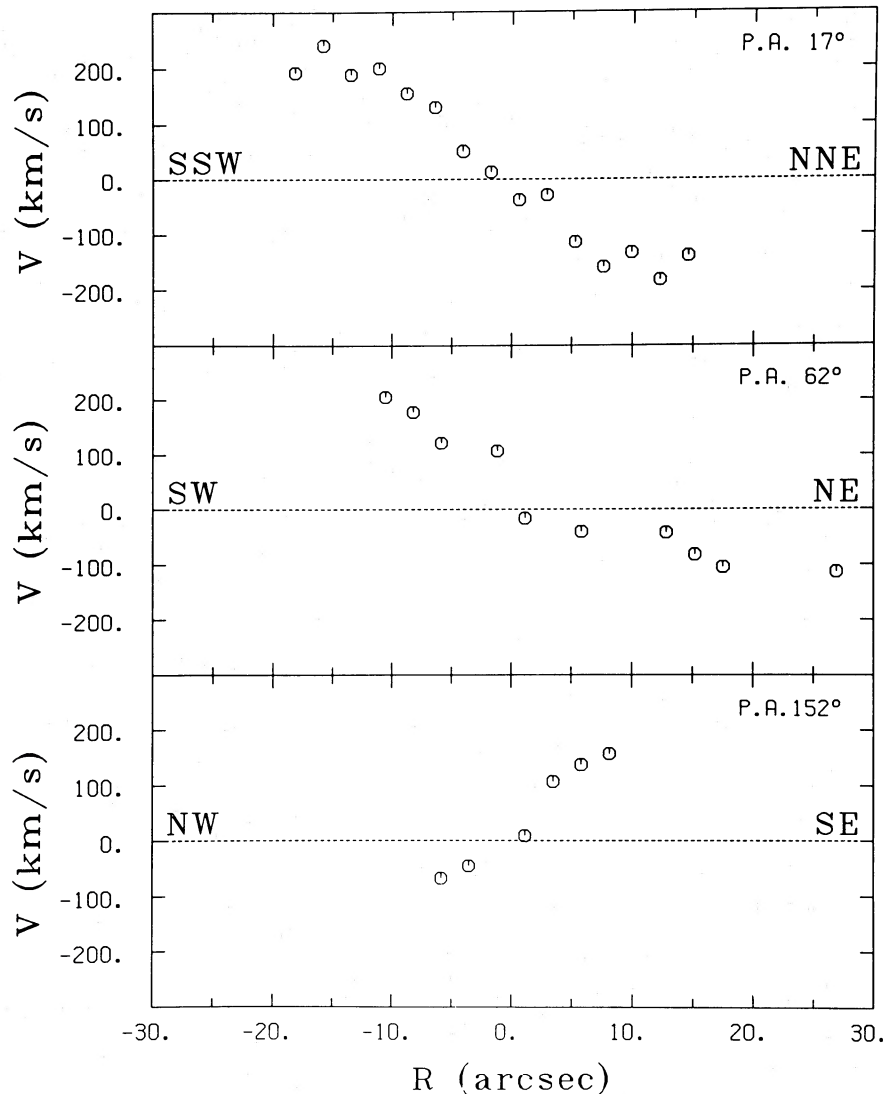


FIG. 8.—The three rotation curves derived from the measurements of the [O III] emission line at P.A. = 17° , 62° , and 152° . Dashed line, central redshift determined from the absorption spectra.

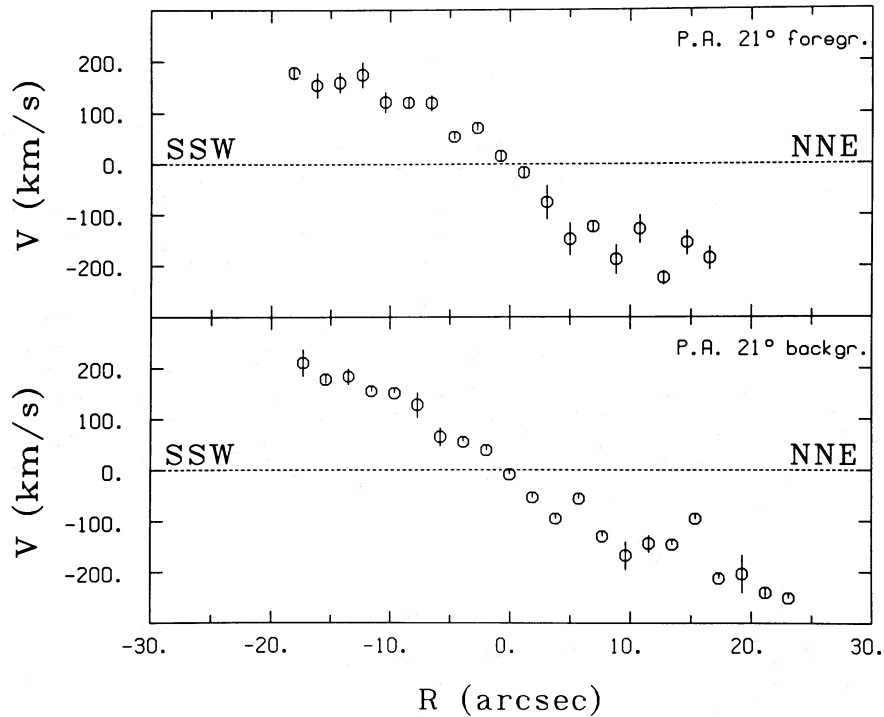


FIG. 9.—The two rotation curves of the gas at P.A. = 21° derived from the [O II] emission line. (top) Foreground of the dust lane; (bottom) background. The error bars show the standard error of the mean velocity.

angles observed at the AAT and ESO are displayed in Figure 10. They were obtained from the analysis of the absorption spectra using the Fourier quotient method. As a check, we also applied the power spectrum method due to Illingworth and Freeman (1974) for the 10 innermost points of P.A. = 107° and found that the agreement was satisfactory. Although a large scatter in velocity dispersion profiles is evident, it seems well established that the central velocity dispersion is $210 \pm 6 \text{ km s}^{-1}$ (slightly higher than Caldwell's 1984 value of 190 km s^{-1} but much lower than the value of ~ 300 found by Möllenhoff and Marenbach 1986) and it shows a tendency to fall with increasing radius, reaching $\sim 100 \text{ km s}^{-1}$ at $|R| = 20''$.

IV. H I EMISSION

NGC 5266 was detected as a 21 cm H I source in a survey of peculiar elliptical galaxies by K. J. Wellington and one of us (D. C.) (unpublished), using the Parkes 64 m antenna. The H I spectral line profile (Figure 11) is broad and double-peaked, suggesting the presence of a rotating disk. The width of the H I distribution is $520 \pm 20 \text{ km s}^{-1}$. The H I velocity extent indicates a projected circular velocity of $\sim 260 \text{ km s}^{-1}$, which is significantly larger than the velocities seen for the ionized gas (Figs. 8 and 9). This suggests that the H I component probably extends beyond the ionized gas, which was detected spectroscopically out to a distance of only $20''$. As the effective radius is around $65''$ – $75''$ (see § II), it is not surprising that the circular velocity continues to rise beyond the limit of the velocity data for the ionized gas. The observed flux represents a total H I mass of $1.75 \times 10^{10} (H/50)^{-2} M_{\odot}$. The ratio M_{HI}/L_B is $0.21 M_{\odot}/L_{\odot}$. To our knowledge, this is the largest amount of H I in an elliptical galaxy detected so far (see Knapp, Turner, and Cunniffe 1985 for the compilation of data). It is an order of magnitude higher than that in the well-known active elliptical galaxy NGC 1052 and also exceeds values in the two “spindle-

like” galaxies with polar disks UGC 7576 and II Zw 73 (Schechter *et al.* 1984) by $\sim 50\%$. Even assuming a high value of $H = 100 \text{ km s}^{-1} \text{ Mpc}^{-1}$, the H I mass in this galaxy is about a factor of 2 larger than in the nearby spirals M33 (Huchtmeier 1973) and NGC 300 (Rogstad, Crutcher, and Chu 1979). If all this gas has been acquired by capturing some spiral galaxy, then it must have been a fairly massive one. It is of interest that this galaxy has not been detected as a radio continuum source. The observations at 2.7 GHz indicate 30 mJy as the upper limit for the flux at this frequency (Sadler 1984).

V. DISCUSSION OF THE OBSERVATIONAL RESULTS

The kinematics of the stellar component of NGC 5266 in many respects resembles that of another elliptical, NGC 5363, with a dust lane cutting its minor axis (Bertola and Galletta 1978; Sharples *et al.* 1983; Bertola, Galletta, and Zeilinger 1985). NGC 5266 shows a rather steep velocity gradient in the central region along the major axis ($23 \text{ km s}^{-1} \text{ arcsec}^{-1}$); its rotation curve then reaches a plateau with $V_{\text{rot}} \approx 140 \text{ km s}^{-1}$ and shows a further rise in velocity beyond $|R| = 25''$. The luminosity-weighted mean velocity dispersion within $|R| = 15''$ is 200 km s^{-1} . All these features mimic NGC 5363 almost exactly, except for the velocity gradient in the central region, which is even higher for that galaxy. The V_m/σ ratio for NGC 5266 is 0.70, almost identical to its counterpart's. The average ellipticity of the isophotes within $R = 15''$ is 0.36. That puts this galaxy on the $(V_m/\sigma, \epsilon)$ -diagram between the lines of isotropic oblate models and triaxial models, the middle axes of which are exactly intermediate between the longest and the shortest ones (Binney 1978; Fig. 12). Three notable differences between this galaxy and NGC 5363 are the cylindrical rotation out to at least $14''$, the possible minor axis rotation in the central region, and the relative direction of the star motions compared with the gas motions in the warps. While the stellar

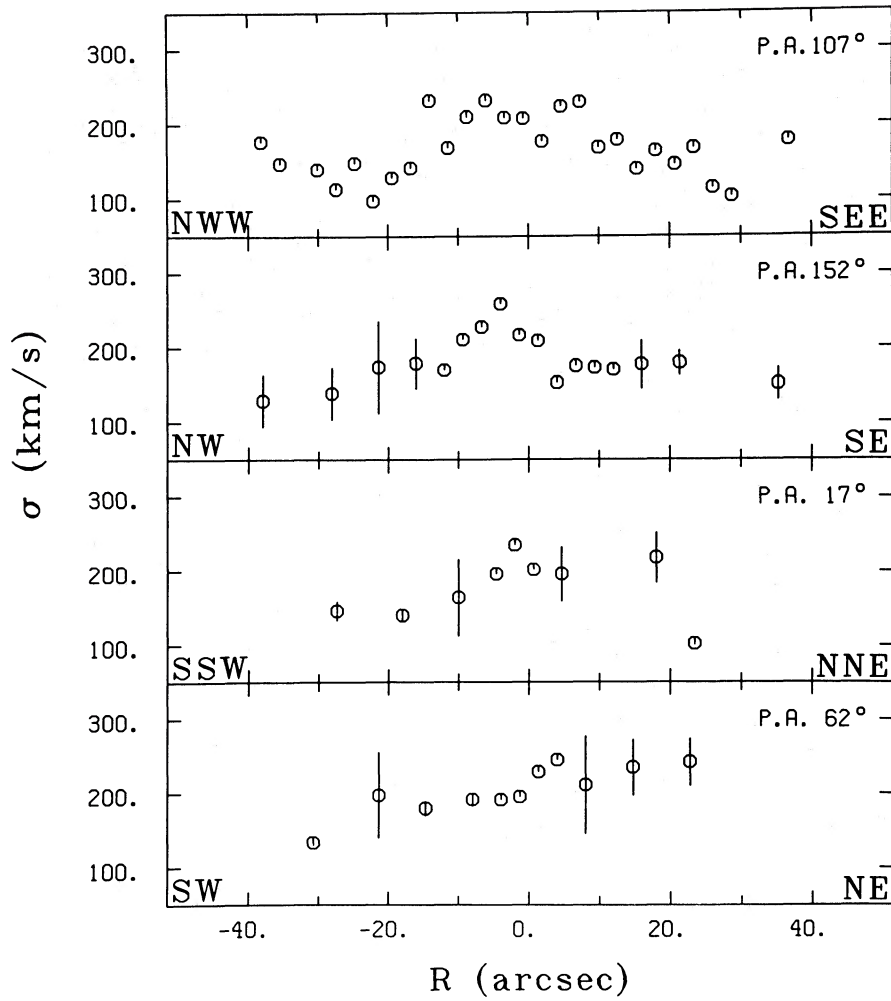


FIG. 10a

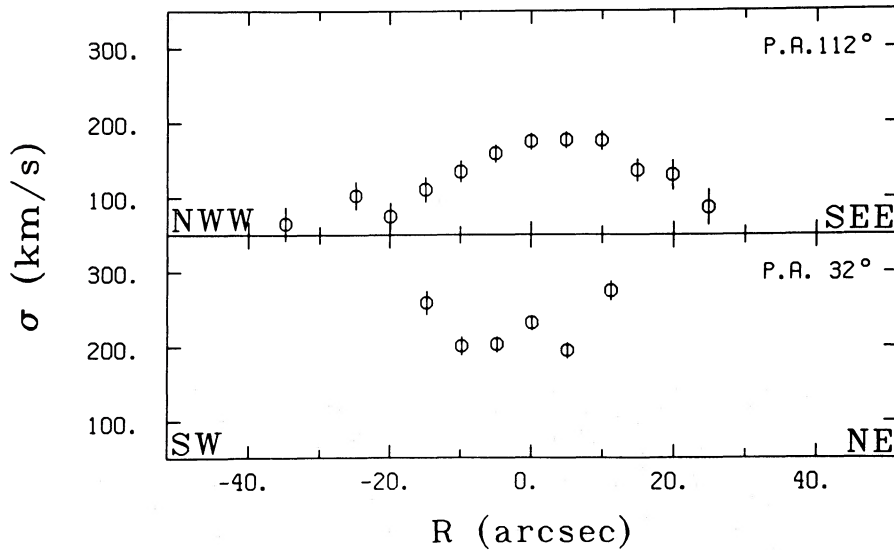


FIG. 10b

FIG. 10.—Velocity dispersion profiles measured from the absorption spectra by the Fourier quotient method (a) AAT data at P.A. = 107°, 152°, 17°, and 62°. Spectra of several rows of the detector have been averaged in the outer regions of P.A. = 17° and 62° to increase the signal-to-noise ratio. The few error bars shown represent the standard error of the mean in the averaged values. (b) ESO data at P.A. = 112° and 32°. The error bars shown reflect the formal errors of the Fourier quotient method.

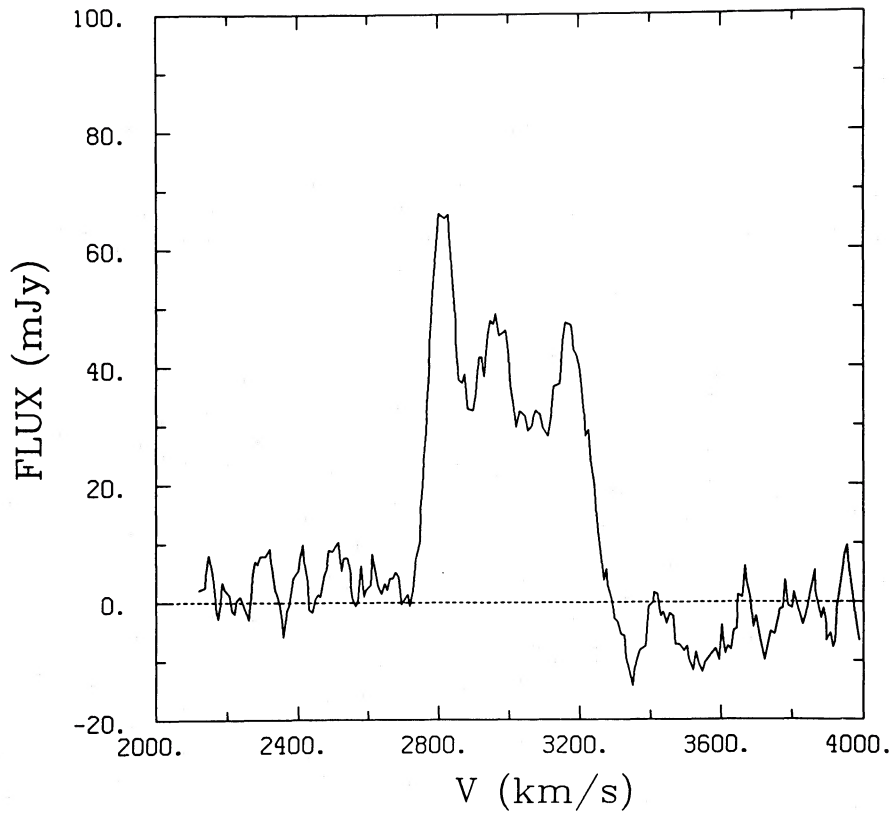


FIG. 11.—H I spectral line profile

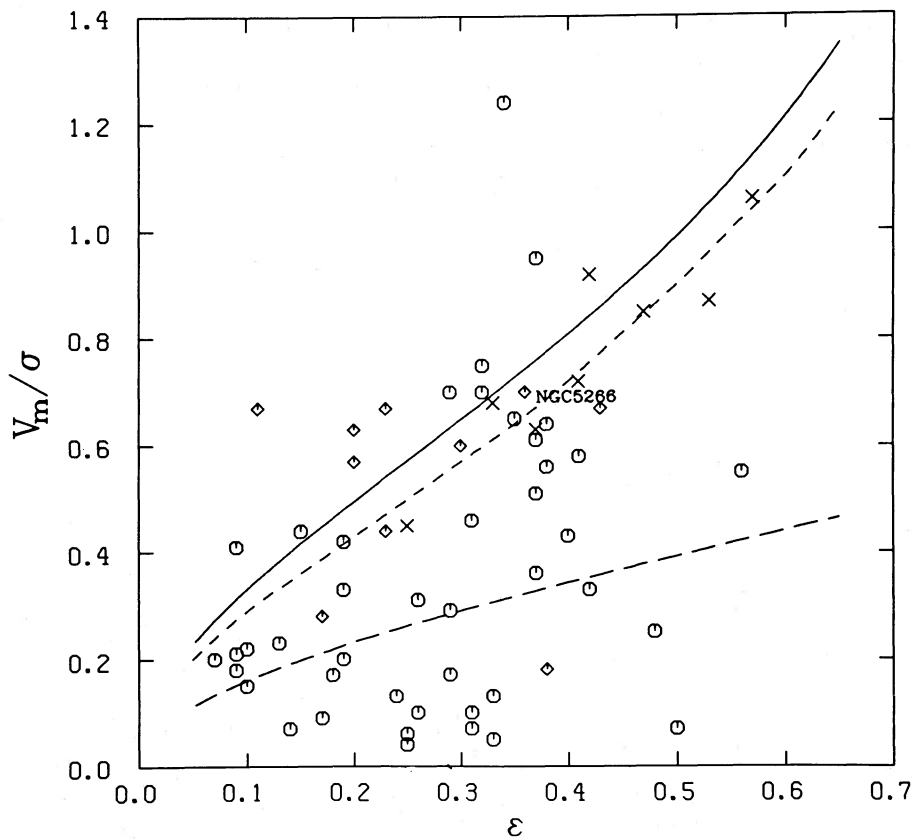


FIG. 12.— V_m/σ vs. ϵ . The curves are the theoretical relationships derived by Binney (1978): *solid line*, isotropic oblate spheroids; *short-dashed line*, isotropic triaxial spheroids with the middle axis exactly intermediate between the short and the long ones; *long-dashed line*, one of the anisotropic oblate spheroids (anisotropy parameters $Q_3 = 2$, $Q_1 = -1$). The data points are taken from the compilation of Davies *et al.* (1983) and a few other sources. *Circles*, normal ellipticals; *crosses*, bulges of the spirals; *diamonds*, dust-lane ellipticals. The position of NGC 5266 is also shown on this diagram.

rotation is seen along the major axis, the rotation of the gaseous disk is in the perpendicular direction in both these galaxies. The presence of the disk, as well as the kinematics of gas and stars, provides clues to the three-dimensional structure of the underlying potential. In this context, Schweizer, Whitmore, and Rubin (1983) discussed three galaxies characterized by them as spindle-shaped with polar rings: NGC 2685, NGC 4650A, and A0136–0801. Since in each of these cases the central velocity dispersion was very low, maximum rotational velocity high, and V_m/σ significantly larger than 1, they concluded that most of these “spindles” are rotationally supported inclined disks. The absence of dust in the “spindle” led them to the belief that these systems are S0 galaxies with rings of gas, dust, and newly formed stars circling in polar orbits. However, the “spindles” of NGC 5266 as well as of NGC 5363 and UKS 0151–498 studied by Sharples *et al.* (1983), are different; they show a rather high global velocity dispersion (200–250 km s⁻¹) and values of V_m/σ consistent with the ellipsoidal models of the stellar component (oblate, prolate, or triaxial). The smooth surface brightness profile, fitting de Vaucouleurs’ $r^{1/4}$ law very well, supports our conclusion that NGC 5266 has no significant stellar disk.

The possible orientations of gas disks in spheroidal potentials have recently been studied by various authors and summarized by Merritt and de Zeeuw (1983). Their analysis of the possible families of orbits indicates that a variety of quasi-stable configurations exists, and it would be difficult to discriminate between different options for one particular galaxy. However, we believe that in this case a number of possibilities can be eliminated and some useful conclusions reached. First, the oblate hypothesis can probably be ruled out: the narrowness of the dust lane and its warp in the north-northeast end shows that the gas must be close to a stable periodic orbit (Lake and Norman 1983), but there are no such orbits around the poles of the oblate spheroid. The second possibility is that the gas disk is in the equatorial plane of a prolate elliptical. The fast major-axis rotation in this galaxy would require large amounts of polar streaming in its prolate body. Richstone and Potter (1982) attempt to construct a stellar dynamical model of the prolate elliptical galaxy with a logarithmic potential, maximized polar streaming, and fixed figure produced $V_m/\sigma = 0.075$. This is significantly less than the observed value for NGC 5266 (0.70). More recently, the analytical study of orbits in a model of a perfect elliptical galaxy by de Zeeuw (1985) has given a further insight into the reasons for this result. He found that there exist only two families of orbits in a stationary perfect prolate galaxy. Both of them are long-axis tubes and cannot give rise to significant streaming along the long axis. Comparisons of de Zeeuw’s (1985) analytical results with numerical orbit calculations in a potential with the density profile closer to the ones derived from the observations of ellipticals (Schwarzschild 1979) showed that these results are not sensitive to the slight variations of the density profile in a model galaxy. The study of preferred orbit planes in generally triaxial galaxies tumbling about the short axis (Steiman-Cameron and Durisen 1984) indicates that introduction of the slow figure tumbling will not allow any appreciable retrograde streaming along the long axis in the inner regions of the prolate galaxy either, while the presence of the prograde streaming in such a model would cause the dust lane to warp in the direction opposite to that which is observed (see below). Thus it seems that the prolate hypothesis for NGC 5266 can be ruled out as well. The third hypothesis is that the stellar body of this

galaxy is triaxial. The possibility that ellipticals are triaxial rather than axisymmetric has been seriously considered ever since it was discovered that many of them are not rotationally flattened (Bertola and Capaccioli 1975; Illingworth 1977). We believe that this galaxy is a particularly strong candidate for being triaxial. The morphology of its dust lane indicates that the gas is near the periodic orbit. Steiman-Cameron and Durisen (1982) have shown that even for a slight deviation from axial symmetry in a nearly oblate potential there exists a significant cross section for the capture of gas into a stable polar orbit. Fast rotation along the major axis of NGC 5266 favors the almost oblate model rather than the prolate model, and so does its position in the $(V_m/\sigma, \epsilon)$ -diagram. Our possible detection of the nonzero minor axis rotation gives further support to the triaxial hypothesis. Therefore, we suggest that the stellar component of NGC 5266 is a nearly oblate triaxial system.

Caldwell (1984), who has also observed this galaxy, reached a similar conclusion independently. However, he was not able to detect any minor axis rotation, so that our result is unconfirmed. Caldwell went further and tried to predict the maximum ratio of the intermediate to the long axis, assuming that the warp in the dust lane shows the direction of the original infall and is the result of the incomplete settling to the preferred plane. Steiman-Cameron and Durisen (1982) give an approximate formula for the maximum angle of orbit to the polar one, at which the particle is still going to precess around the longest axis:

$$I = \arcsin \{ [1 - (b/a)^2] / [1 - (c/a)^2] \}^{1/2}, \quad (2)$$

where $a > b > c$ are the semiaxes of the spheroid. Using this formula, Caldwell (1984) finds, for the observed values of $c/a = 0.65$ and $i = 25^\circ$, that b/a should not exceed 0.95. Strictly speaking, as was pointed out by Steiman-Cameron and Durisen (1982), equation (2) is valid only for almost spherical systems (b/a and $c/a \approx 1$), while NGC 5266 is quite significantly flattened. More importantly, however, there is as yet no strong evidence that warped disks result from incomplete settling. The only published model that we are aware of that attempts to show this (Tubbs 1980) did not consider dissipation, which is essential for the physics of the settling-down process. Tubbs (1980) attempted to model the dust lane in Cen A as a transient feature; however, we believe that the thin gas disk in NGC 5266 is settled because its morphology and kinematics are well ordered. An alternative explanation of the warped dust lanes was suggested by van Albada, Kotanyi, and Schwarzschild (1982, hereafter vAKS). Unpublished orbit calculations of D. Merritt, and their own analytical treatment, showed that, in a triaxial potential tumbling around its shortest axis, there exists a family of stable periodic orbits which are tilted away from the minor axis and that the tilt increases with radius. They argued that the warp in the dust lanes of some elliptical galaxies (e.g., Cen A and M84) is due to the slow tumbling motion of the triaxial figure around its shortest axis. However, these anomalous tilted orbits are stable only if the figure tumbles in the retrograde sense to the motions of gas. The discovery that the stellar motions are not retrograde but rather prograde led Caldwell (1984) to reject this model. However, as pointed out by Steiman-Cameron and Durisen (1984) and Bertola, Galletta, and Zeilinger (1985), one should make a distinction between the streaming of the stars in the figure and the possible tumbling of the whole figure itself. It is conceivable that the directions of the two motions could be

opposite. In fact, stellar dynamical models of tumbling homogeneous ellipsoidal systems with some regions of retrograde streaming have already been constructed (Freeman 1966), as well as for the realistic density distributions appropriate for elliptical galaxies (Schwarzschild 1982).

VI. MODELS OF THE GAS DYNAMICS

To understand the settling down of a gas disk which is originally away from the preferred plane, we decided to run a few time-dependent simulations using particle methods. The detailed description of the method will be presented elsewhere (Varnas 1986), so here we restrict ourselves to a brief outline of the procedure and the tests. Essentially this code is similar to the one used by Tubbs (1980) with one important improvement—it incorporates dissipation. At the start of the simulation we usually have an ensemble of non-self-gravitating particles distributed randomly in the plane of the disk, with rotational velocities to balance the centrifugal force due to the spheroidal potential in which the disk sits and velocity dispersions of the order of 10 km s^{-1} along the X , Y , and Z axes. The particles are advanced using the second-order time-centered “leap-frog scheme,” then their velocities are smoothed over a length scale H . A similar method has been used to simulate viscosity in plasma models by Marder (1975), but our smoothing procedure differs from his. Instead of interpolating the velocities to the grid we use the method of kernel estimates (Gingold and Monaghan 1982) to work out the smoothed velocities V_s of each particle. This insures that the scheme conserves angular momentum, while Marder’s method does not. Having the smoothed velocity of the particle i , its new velocity is

$$V_i - \gamma(V_i - V_{is}), \quad (3)$$

where V_i is particle’s velocity after the first updating due to gravity and γ is a coefficient describing the fraction of the total smoothing used. The quantity γ is a function of the time step used in the integration and also of another parameter α , which is the analog of the viscosity coefficient. Typically, $\gamma \approx 0.1$, which means that we have $\sim 10\%$ smoothing over a certain length scale.

This scheme has two free parameters: the smoothing length H and the viscosity coefficient α , which have to be appropriately calibrated. The choice of H is determined by the observed value of the velocity dispersion of H I clouds in the disks of the spiral galaxies. The latest measurements (van der Kruit and Shostak 1983) give values of $7\text{--}10 \text{ km s}^{-1}$. We adopted the upper value. Knowing the velocity dispersion allows us to estimate the maximum radial excursion of the particle orbits at different radii, which is a measure of the length scale over which collisions between the clouds are effective in smoothing the velocity field. In choosing the smoothing length H , we adopted the procedure described by Tohline, Simonson, and Caldwell (1982, hereafter TSC), which they used to estimate the average distance between the adjacent rings of matter “communicating” with each other. This determined the time scale of the differential precession of those rings. Having estimated this time scale, we then required that the settling-down time scale be as close as possible to it by adjusting the viscosity coefficient.

Part of the code, excluding the dissipation, was tested by reproducing Tubbs (1980) model of Cen A. The evolution of the ensemble of particles distributed in the disk, which was originally inclined by 30° to the equatorial plane of the under-

lying prolate potential, was followed for a time period of order 10^9 yr . The morphology of the particle distribution at two stages of the evolution, corresponding to the ones shown by Tubbs (1980), $t = 0.3$ and $1.0 \times 10^9 \text{ yr}$, was very similar to his.

We then used an oblate mass model with density profile following the modified Hubble law:

$$\sigma = \rho_0 [1 + (R/a)^2 + (Z/b)^2]^{-3/2}. \quad (4)$$

The differential precession times for the sequence of pairs of rings at different radii separated by the smoothing length H have been estimated approximately, analytically. The numerical calculation of these times was performed by evolving rings of particles until their lines of nodes moved by $\pi/2$. That gave us the numerical estimates of precession rates, which in turn allowed us to compute the differential precession times at different radii. The agreement with the analytical calculations over the interval of radii of interest was very good. Having reliable estimates of the differential precession times, we could then calibrate the viscosity coefficient α . To do this, we generated an ensemble of particles distributed uniformly in a disk inclined to the equatorial plane at the same angle as the rings for the differential precession calculation. This time the evolution of the system was followed with dissipation, and the growth of the settled disk in the equatorial plane of the potential well was monitored. TSC argued that, when the angle between the line of nodes of the two interacting rings of matter gets sufficiently large (e.g., $\pi/2$), the collisions between the clouds in different rings destroy the rings’ angular momentum component parallel to the equatorial plane. This forces “clouds” to settle to the equatorial plane of the potential. From this argument, it is clear that the settling-down time should be equal to the differential precession time for the rings of matter separated by the characteristic length scale—the smoothing length H . Therefore, we varied the coefficient α until we got the rate of the growth of the radius of the settled disk closely following the relationship between the radius and the differential precession time.

As a test of consistency we checked the conservation of the particles’ Z -component of the angular momentum, which was parallel to the potential’s axis of symmetry: it was conserved within a fraction of 1%. We also checked what importance dissipation has in the evolution of this system, compared to the gravity of the underlying potential. We certainly did not want it to be the dominating factor. In fact, we found that the smoothing procedure at each time step changed particle velocities on average by only a fraction of the amount that they were changed due to the gravitational force of the potential well (typically 10%–20%). We judged these tests as sufficient to establish the credibility of the results produced by this code.

Next, we had to choose the mass model for NGC 5266. We wanted a nearly oblate triaxial potential. The model constructed by Schwarzschild (1979) was chosen because it has a realistic density profile similar to that given by equation (4) and has been shown to be fully self-consistent and stable (Smith and Miller 1982). Since the original mass model was not easily adaptable for different ellipticities, Schwarzschild derived approximate analytical expressions for his model. (The actual expressions for the potential and density distribution have been reported in de Zeeuw and Merritt 1983, Appendix B.) We adapted this simplified model to represent the potential of the stellar component of NGC 5266. The central density was adjusted to produce a peak rotational velocity of 250 km s^{-1} around the longest axis, corresponding to the observed gas

rotation. The major to minor axis ratio was constant for all models ($p = 1.55$), corresponding to the observed ellipticity (we assumed that the shortest axis of the potential is in the plane of the sky, since the apparent rotation of the stellar component is so unusually high for an elliptical that significant inclination of the rotation axis to the plane of the sky seems unlikely). The length of the intermediate axis was varied and the differences in the evolution of the gaseous disk followed.

One of our first simulations used parameters suggested by Caldwell (1984). The original inclination of the disk of particles was 25° away from the polar orbit, the ratio of the intermediate to short axis $q = 1.46$, corresponding to $\sim 5\%$ triaxiality of the potential. At the start of the simulation, 5000 particles were originally distributed uniformly in the disk between radii of 1 and 5 kpc and given rotational velocities to balance the centrifugal force plus small velocity dispersion. In the center of the potential there was a "hole" with a radius of 450 pc. Particles getting into this region were considered "swallowed" by the nucleus and were removed from the subsequent calculation. Almost 40% of all particles had fallen into this "hole" by $T = 4.6 \times 10^9$ yr in this simulation. Four frames of the evolution of this disk are displayed in Figure 13. The size of the whole window is 14 kpc, time T is measured in 10^9 yr. The

projection of the particle distribution on the (X, Z) -plane is shown here. The X , Y , and Z axes are the long, intermediate, and short axes correspondingly. From these pictures several conclusions can be drawn. First, this disk is not settling down to the polar orbit around the (longest) X -axis of the potential, but rather around the (shortest) Z -axis. Clearly, the potential is not sufficiently triaxial to capture gas into a polar orbit from the original 25° inclination. Second, the rings' coherency times at these radii are so short that the original disk is dispersed very quickly—over $\sim 10^8$ yr. Third, the small disk settles down to the principal plane (X, Y) on a short time scale ($T < 10^9$ yr) even from the original inclination of the disk as high as 65° . However, the subsequent growth of its radius proceeds very slowly. This can be explained from the dependence of the differential precession time $\tau = f(R, \Theta)$, where Θ is the original inclination of the disk to the equatorial plane and R is the radius. Figure 3 in TSC shows that, for small R , τ varies very little with Θ (they showed $\Theta = 10^\circ$ and 40° curves), but for larger radii the differences in settling-down times are becoming significant.

To get the particles to settle down into a polar orbit we decided to shorten somewhat the intermediate axis of the triaxial spheroid. In our next simulation, the initial conditions for

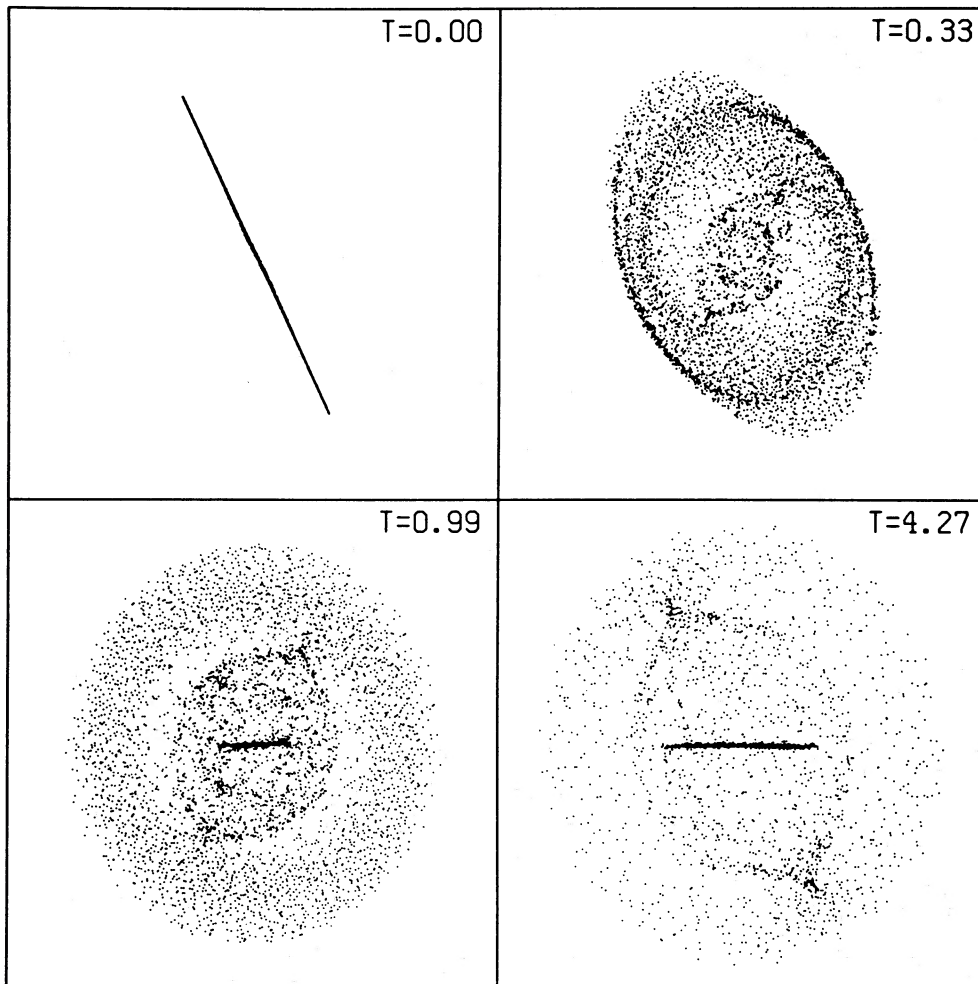


FIG. 13.—The four frames of the evolution of the gas disk in a stationary nearly oblate potential with 5% triaxiality. Time T in 10^9 yr, size of window 14 kpc. The longest axis (X) is in the horizontal direction and the shortest (Z) is in the vertical direction.

the particles are the same but the ratio of the intermediate to short axes $q = 1.40$, making the potential $\sim 10\%$ triaxial. Six frames of the evolution of this system are shown in Figure 14 (all scales and projections are the same as in Fig. 13). It is immediately obvious that the small change in axial ratio has entirely changed the evolution of the disk. In this case large numbers of particles have eventually settled into the polar orbit around the (longest) X -axis of the potential well after $T = 2 \times 10^9$ yr. The infall of gas to the nucleus was 24% of the original mass at $T = 4.3 \times 10^9$ yr. Another important feature of this simulation is that no significant warp in the settled disk was observed at any stage. Although short warps at the ends of the settling disk did appear occasionally (as at $T = 2.31$), they were no indication of the direction of the original infall, because on the time scale needed for the part of the gas to settle down it loses its memory about this direction. In other words, the planes of the orbits of the outermost particles have already precessed over a significant angle by that time.

After these unsuccessful attempts to model the warped dust lane in NGC 5266 as a result of the incomplete settling to the polar orbit of the stationary triaxial potential, we decided to explore the alternative model proposed by vAKS. We took the same mass model as in the previous simulation, but this time the potential was allowed to tumble very slowly around the shortest axis and in a retrograde sense to the observed streaming. The chosen tumbling is so small (the period $T = 4.4 \times 10^9$

yr) that it would probably have almost no effect on the large streaming velocities observed in this galaxy. The velocity of the stars at $R = 7$ kpc due to the figure rotation would be just ~ 10 km s $^{-1}$, while the observed velocities at this radius are ~ 200 km s $^{-1}$. The particles were originally distributed in a disk with the maximum radius of 6 kpc which was exactly in polar orbit if the potential was stationary. The calculation was performed in a rotating frame of reference with inertial forces incorporated explicitly into the equations. The infall of particles to the nucleus was only 10% at $T = 4.5 \times 10^9$ yr. Four frames of the evolution of this system are shown in Figure 15. The orientation of the axes and the projections displayed are the same as in Figures 13 and 14. From these pictures we can see that the tumbling of the potential originally disperses a large amount of particles over a significant volume, but after $2\text{--}3 \times 10^9$ yr, due to the dissipative forces, most of the particles settle down into a warped disk rotating around the longest axis. Although the warp was retained until the calculation was terminated ($T = 5.54 \times 10^9$ yr), the appearance of the settled disk in this model varied slightly all the time, contrary to the conclusions of some other workers (e.g., vAKS) that such features should be stationary. Their argument was based on the calculations of the periodic orbits in conservative systems. Adding dissipation changes the behavior of particle orbits. The important thing is that there is a redistribution of the angular momentum in this quasi-settled disk. Some particles are moving inward, others

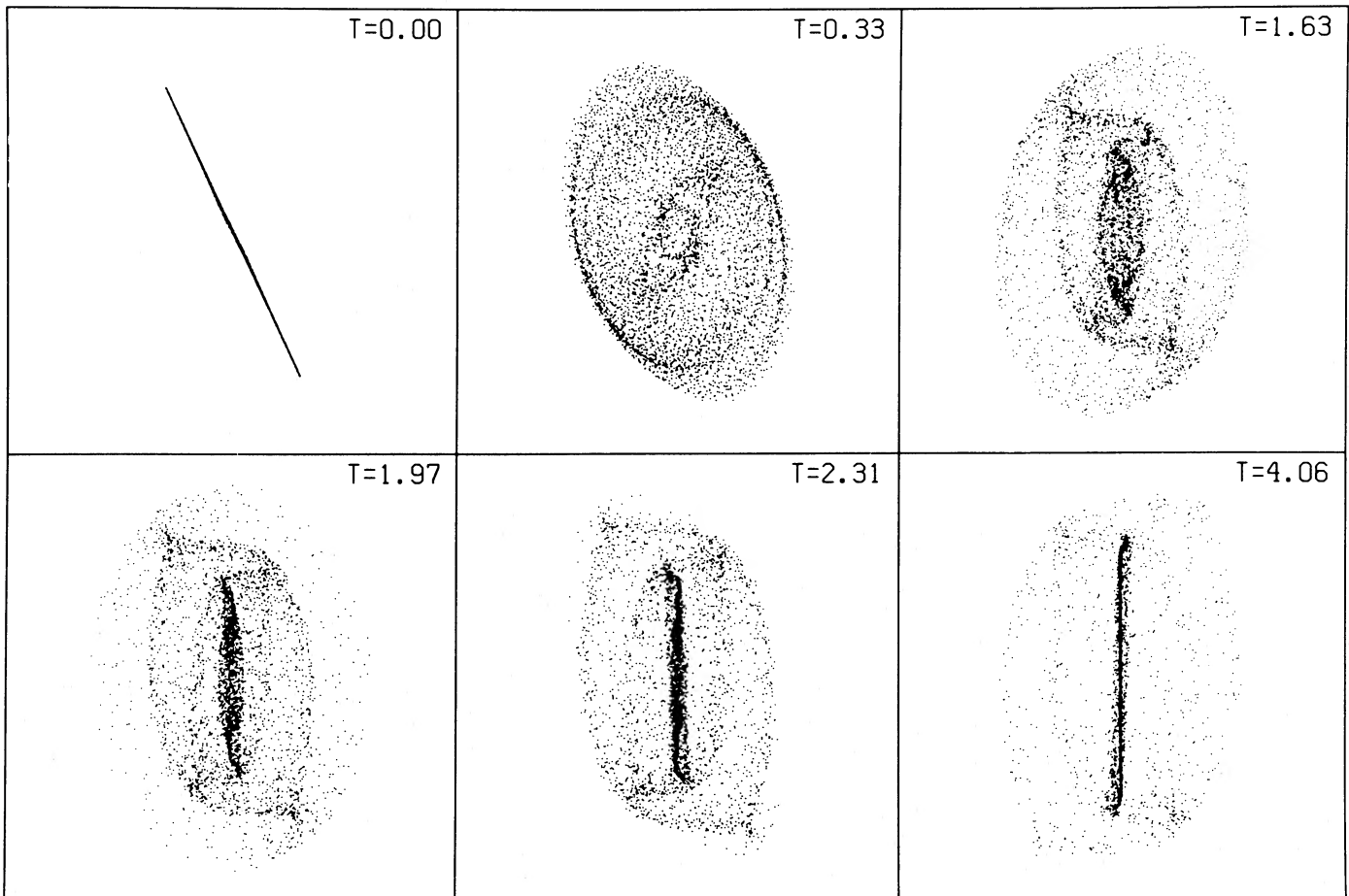


FIG. 14.—The six frames of the evolution of the same disk as in Fig. 13 in a stationary 10% triaxial potential. All scales and projections are the same as in Fig. 13.

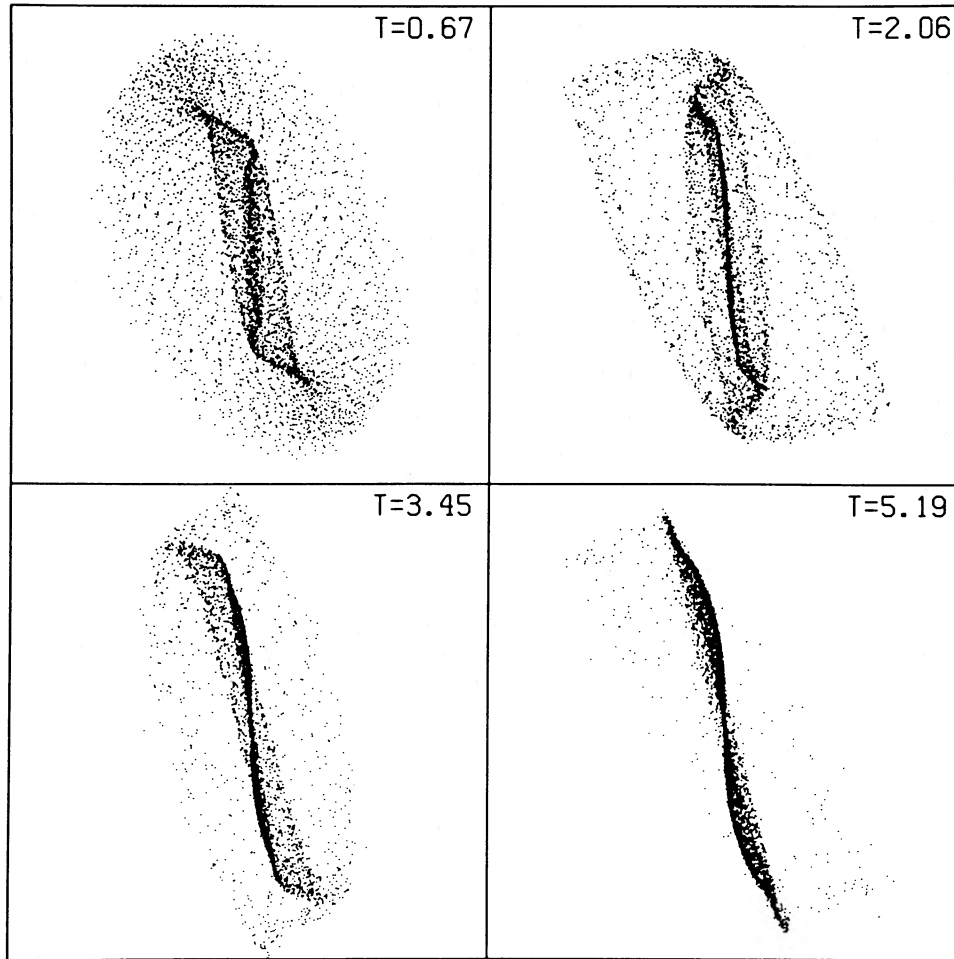


FIG. 15.—The four frames of the evolution of the disk in the same potential as in Fig. 14 but slowly tumbling around the Z -axis with the angular momentum vector pointing down the page. The system of coordinates rotates with the potential. All projections are the same as in Figs. 13 and 14.

move outward. Since the inclination of the simple periodic orbit (i.e., preferred plane for the gas to settle) increases with radius, the orbit whose radius varies with time continues to precess and never settles down to any preferred plane. Closer study of the shape of this disk shows that not only does it warp with increasing $|Z|$, but it also twists with increasing $|Y|$. This twisting makes our warped disk look rather broad while viewing it “edge-on,” as in Figure 15. In Figure 16 we attempted to make a direct comparison of the warped disk produced in our simulation with the actual appearance of the dust in NGC 5266. To achieve the best match we rotated the coordinate system over $\phi = 10^\circ$ around the Z -axis and $\theta = 17^\circ$ around the new Y -axis and removed all the particles found in a cylinder of radius $R = 3$ kpc (this is the observed radius of the inner boundary of the annulus of dust in this galaxy, assuming the distance modulus 56 Mpc and the axis of symmetry to be the longest axis of the elliptical component), as well as the ones with Y -coordinate exceeding 2.8 kpc (behind the stellar body). We assumed that in our picture gas and dust clouds represented by those particles would be invisible because of the light of stars in front of them. We found that this picture matches most of the observed features reasonably well. The regions densely covered by particles are the most likely ones to be visible. This is nearly the exact appearance of the dust lane on our pho-

tograph of NGC 5266 (Fig. 1). In the front edge of the annulus the density of the particles in the line of sight seems to increase to the south of the nucleus, because the twisting of the disk makes us see it almost edge-on at this end. That is also where we observed higher intensity in $[\text{O III}]$ emission (the slit was positioned on the front edge of the annulus). Stronger emission in $[\text{O III}]$ and $\text{H}\beta$ in this region has also been noted by Caldwell (1984). In our Taurus data, a few knots of emission detected were concentrated east of the northern edge of the annulus, and a couple were located west of the southern end. This is also confirmed by gas rotation curves from slit spectroscopy. The extent of detected emission is much larger in $\text{P.A.} = 62^\circ$ (particularly in the northeast) than in $\text{P.A.} = 152^\circ$. This asymmetry is very well accounted for in our model (Fig. 16), which produces a higher concentration of particles in the areas where the emission is stronger and gas densities probably higher.

VII. IMPLICATIONS FOR STELLAR DYNAMICAL MODELS

Having studied the gas dynamics in NGC 5266, we now discuss the implications of our models for the dynamics of the stellar component in this galaxy. Realistic numerical stellar dynamical models of elliptical galaxies are still at an early stage. There are two lines of approach to this modeling: large-

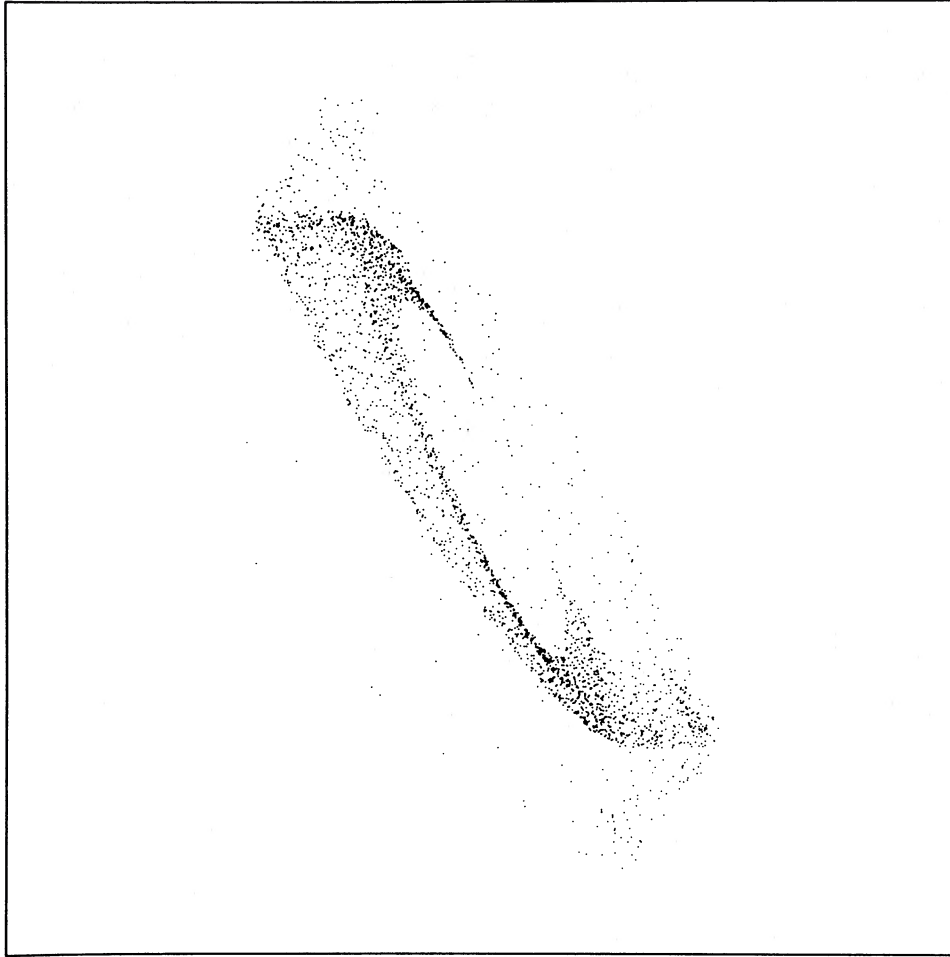


FIG. 16.—A special projection of one of the frames ($T = 3.45$) in our tumbling model to match the appearance of the dust lane in NGC 5266. The size of the frame is 16 kpc. North is to the top and west to the right.

scale N -body simulations of self-gravitating particles with some reasonable initial conditions (Miller and Smith 1979; Wilkinson and James 1982; Negroponte and White 1983), and the self-consistent field method, based on the calculations of individual orbits in a given potential (Schwarzschild 1979, 1982; Richstone 1980; Richstone and Potter 1982; de Zeeuw *et al.* 1983). The latter seems to offer certain advantages, because here one deals directly with the orbit families and has a better understanding of the kinematics needed to construct galaxies with such prescribed features as the density distribution, the three-dimensional shape, streaming velocities, pattern rotation, and velocity dispersions. An attempt to construct a self-consistent prolate mass model with large streaming velocities (Richstone and Potter 1982) for the “spindle-shaped” galaxy NGC 2685 has already been mentioned above. The triaxial models with slow figure rotation constructed by Schwarzschild (1982) seem to be more promising for our galaxy. These have a density distribution with the modified Hubble profile and axis ratio 1:1.25:2 ($X > Y > Z$). The figure was slowly tumbling (rotation period $T = 1.2 \times 10^9$ yr) around the (shortest) Z -axis. The analysis of orbits in this potential has shown that three major orbit families dominate the phase space in such a potential: the box orbits, two branches of X -tubes circling the longest X -axis and inclined to the (Y, Z)-plane, and the

Z -tubes which circle the (shortest) Z -axis. Schwarzschild argued that out of these orbit families only the Z -tubes can supply significant streaming in the figure along the (longest) X -axis. In fact, he has actually shown what a dramatic effect on streaming the introduction of Z -tubes has (compare his model D with model C). However, Schwarzschild was interested in constructing a model with high prograde streaming and therefore excluded from his calculation the retrograde Z -tubes, which also exist outside Binney’s instability strip. In his mass model, that region was limited to the area within $R \approx 2$ kpc, but it is much larger for the mass model of NGC 5266 used in our simulations, since this model tumbles much slower and is significantly rounder in the (X, Y)-plane. We have estimated the boundaries of Binney’s instability strip for this model, using expressions for the tilt angles of the planes of anomalous orbits given by David, Steiman-Cameron, and Durisen (1985). The instability strip falls between the radii of 9 and 11.5 kpc. This means that our observed rotation curves barely reach the inner boundary of the Binney’s instability strip if our mass model of this galaxy is correct ($R = 35''$ corresponds to 9.5 kpc for $H = 50 \text{ km s}^{-1} \text{ Mpc}^{-1}$). Therefore, retrograde Z -tubes will be stable in the observed region. It should also be noted that the X -tubes in the inner regions and box orbits in the outer regions will also contribute to the retrograde streaming, as was

shown by Schwarzschild (1982). It would be interesting to see if a self-consistent, slowly tumbling, nearly oblate model with large retrograde streaming could be constructed using those three major orbit families: box orbits, X -tubes, and retrograde Z -tubes. Vietri (1986) has recently attempted to construct a self-consistent triaxial model tumbling in the direction retrograde to the stellar streaming from the bulge of our galaxy. He failed to achieve the desired result for two reasons. First, the family of retrograde Z -tubes, which are elongated along the intermediate axis, opposed the shape of the triaxial bar and, consequently, the usage of those orbits was restricted. Second, the figure of his model was tumbling so fast (nearly 50 times faster than our model of NGC 5266) that any retrograde orbits present in the model could only manage to decrease somewhat the huge overall rotation, rather than change its direction. We believe that the quantitative differences of this model from that of NGC 5266 proposed by us are so large, that drawing any analogies between them can be quite misleading.

If our model is correct, the presence of stellar counter-streaming, retrograde with respect to a slow rotation of the whole galaxy figure, could possibly also be used to interpret the observations of the prograde warps in NGC 5128 and UKS 0151–498 (Bertola, Galletta, and Zeilinger 1985) and of H I disks in NGC 4278 (Knapp 1983) and NGC 3998 (Knapp, van Driel, and van Woerden 1985). On the other hand, the explanation of the retrograde warps in NGC 5363 (Bertola, Galletta, and Zeilinger 1985) does not require the presence of counter-streaming. The possibility that these warps are the outcome of the incomplete settling of gas to the preferred plane of a stationary ellipsoidal potential cannot be ruled out on the basis of the two unsuccessful models of this kind presented in this paper. However, these two examples tell us that the plausibility of such an explanation, which has been taken for granted in the past, should be seriously questioned.

VIII. CONCLUSIONS

Results of our observations and dynamical modeling of NGC 5266 lead us to the following conclusions about the nature of this galaxy. It is a fast and cylindrically rotating elliptical galaxy. Its three-dimensional shape is probably triaxial (nearly oblate). The dust lane cutting its minor axis discloses a warped gas disk, which is likely to be a remnant of a massive gas-rich spiral galaxy captured into polar orbit of the elliptical component. The warp in the gas disk of NGC 5266 probably does not tell us anything about the original direction of the infall of gas and consequently cannot be used to put a lower limit on the triaxiality of the figure. We believe that it would be difficult to produce the observed warp in a stationary triaxial potential. It seems to us that the slow tumbling of the figure retrograde to the streaming motions of the stars is more likely to give a satisfactory explanation of the morphology of gas in this galaxy.

We would like to thank Dr. K. Taylor for helping us with the Taurus observations and its data reduction, Dr. C. Carignan for making one of his data reduction programs available to us, and Mr. D. Malin for preparing the unsharp masked print in Figure 1. The Padova Observatory Fourier quotient reduction programs were set up by D. Barceloux on the basis of a version kindly provided by J. Rose. F. B. thanks the AAT photography service for kindly obtaining the deep plate of NGC 5266. S. R. V. would like to thank Dr. J. J. Monaghan for continued interest and guidance through the course of this work, Dr. M. P. Schwarz for numerous stimulating discussions on galactic dynamics, and Dr. R. M. Sharples for useful advice on data reduction techniques. He also acknowledges the assistance of the Commonwealth Post-Graduate Research Award.

REFERENCES

- Atherton, P. D., Taylor, K., Pike, C. D., Harmer, C. F. W., Parker, N. M., and Hook, R. N. 1982, *M.N.R.A.S.*, **201**, 661.
 Bertola, F., and Capaccioli, M. 1975, *Ap. J.*, **200**, 439.
 Bertola, F., and Galletta, G. 1978, *Ap. J. (Letters)*, **226**, L115.
 Bertola, F., Galletta, G., and Zeilinger, W. W. 1985, *Ap. J. (Letters)*, **292**, L51.
 Binney, J. 1978, *M.N.R.A.S.*, **183**, 501.
 Caldwell, N. 1984, *Ap. J.*, **276**, 96.
 Carter, D., Jenkins, C. R., and Sadler, E. 1985, in preparation.
 David, L. P., Steiman-Cameron, T. Y., and Durisen, R. H. 1985, *Ap. J.*, **295**, 65.
 Davies, R. L., Efstathiou, G., Fall, S. M., Illingworth, G., and Schechter, P. L. 1983, *Ap. J.*, **266**, 41.
 de Vaucouleurs, G. 1948, *Ann. d'Ap.*, **11**, 247.
 de Vaucouleurs, G., de Vaucouleurs, A., and Corwin, H. G. 1976, *Second Reference Catalog of Bright Galaxies* (Austin: University of Texas Press), p. 196.
 de Zeeuw, T. 1985, *M.N.R.A.S.*, **216**, 273.
 de Zeeuw, T., Franx, M., Meys, J., Brink, K., and Habing, H. J. 1983, in *IAU Symposium 100, Internal Kinematics and Dynamics of Galaxies*, ed. E. O. Athanassoula (Dordrecht: Reidel), p. 285.
 de Zeeuw, T., and Merritt, D. 1983, *Ap. J.*, **267**, 571.
 Ebner, K., and Balick, B. 1985, *A.J.*, **90**, 183.
 Freeman, K. C. 1966, *M.N.R.A.S.*, **134**, 1.
 Gingold, R. A., and Monaghan, J. J. 1982, *J. Comp. Phys.*, **46**, 429.
 Graham, J. A. 1979, *Ap. J.*, **232**, 60.
 Gunn, J. E. 1979, in *Active Galactic Nuclei*, ed. C. Hazard and S. Mitton (Cambridge: Cambridge University Press), p. 213.
 Hawarden, T. G., Elson, R. A. W., Longmore, A. J., Tritton, S. B., and Corwin, H. G., Jr. 1981, *M.N.R.A.S.*, **196**, 747.
 Huchtmeier, W. 1973, *Astr. Ap.*, **22**, 91.
 Illingworth, G. 1977, *Ap. J. (Letters)*, **218**, L49.
 Illingworth, G., and Freeman, K. C. 1974, *Ap. J. (Letters)*, **188**, L83.
 Knapp, G. R. 1983, in *IAU Symposium 100, Internal Kinematics and Dynamics of Galaxies*, ed. E. O. Athanassoula (Dordrecht: Reidel), p. 297.
 Knapp, G. R., Turner, E. L., and Cuniffe, P. E. 1985, *A.J.*, **90**, 454.
 Knapp, G. R., van Driel, W., and van Woerden, H. 1985, *Astr. Ap.*, **142**, 1.
 Kotanyi, C. G., and Ekers, R. D. 1979, *Astr. Ap.*, **73**, L1.
 Lake, G., and Norman, C. 1983, *Ap. J.*, **270**, 51.
 Malin, D. F. 1979, *Nature*, **277**, 279.
 Marder, B. M. 1975, *Math Comp.*, **29**, 434.
 Merritt, D., and de Zeeuw, T. 1983, *Ap. J. (Letters)*, **267**, L19.
 Miller, R. H., and Smith, B. F. 1979, *Ap. J.*, **227**, 785.
 Möllenhoff, C. 1982, *Astr. Ap.*, **108**, 130.
 Möllenhoff, C., and Marenbach, G. 1986, *Astr. Ap.*, **154**, 219.
 Negroponte, J., and White, S. D. M. 1983, *M.N.R.A.S.*, **205**, 1009.
 Richstone, D. O. 1980, *Ap. J.*, **238**, 103.
 Richstone, D. O., and Potter, M. D., 1982, *Nature*, **298**, 728.
 Rogstad, D. H., Crutcher, R. M., and Chu, K. 1979, *Ap. J.*, **229**, 509.
 Sadler, E. M. 1984, *A.J.*, **89**, 53.
 Sargent, W. L. W., Schechter, P. L., Bokserberg, A., and Shortridge, K. 1977, *Ap. J.*, **212**, 326.
 Schechter, P. L., and Gunn, J. E. 1978, *A.J.*, **83**, 1360.
 Schechter, P. L., Sancisi, R., Van Woerden, H., and Lynds, C. R. 1984, *M.N.R.A.S.*, **208**, 111.
 Schwarzschild, M. 1979, *Ap. J.*, **232**, 236.
 ———. 1982, *Ap. J.*, **263**, 599.
 Schweizer, F. 1980, *Ap. J.*, **237**, 303.
 Schweizer, F., Whitmore, B. C., and Rubin, V. C. 1983, *A.J.*, **88**, 909.
 Sharples, R. M., Carter, D., Hawarden, T. G., and Longmore, A. J. 1983, *M.N.R.A.S.*, **202**, 37.
 Smith, B. F., and Miller, R. H. 1982, *Ap. J.*, **257**, 103.
 Steiman-Cameron, T. Y., and Durisen, R. H., 1982, *Ap. J. (Letters)*, **263**, L51.
 ———. 1984, *Ap. J.*, **276**, 101.

- Tohline, J. E., Simonson, G. F., and Caldwell, N. 1982, *Ap. J.*, **252**, 92 (TSC).
Tonry, J., and Davis, M., 1979, *A.J.*, **84**, 1511.
Tubbs, A. D. 1980, *Ap. J.*, **241**, 969.
van Albada, T. S., Kotanyi, C. G., and Schwarzschild, M. 1982, *M.N.R.A.S.*, **198**, 303 (vAKS).
van der Kruit, P. C., and Shostak, G. S. 1983, in *IAU Symposium 100, Internal Kinematics and Dynamics of Galaxies*, ed. E. O. Athanassoula (Dordrecht: Reidel), p. 69.
- Varnas, S. R. 1986, in preparation.
Vietri, M. 1986, *Ap. J.*, **306**, 48.
Wilkinson, A., and James, R. A. 1982, *M.N.R.A.S.*, **199**, 171.
Wilkinson, A. A., Sharples, R., Fosbury, R. A. E., and Wallace, P. T. 1986, *M.N.R.A.S.*, **218**, 297.

F. BERTOLA: Istituto di Astronomia, Universita' di Padova, vicolo dell'Osservatorio, 5, I 35122 Padova, Italy

D. CARTER and K. C. FREEMAN: Mount Stromlo and Siding Spring Observatories, Private Bag, Woden P.O., A.C.T. 2606, Australia

G. GALLETTA: Osservatorio Astronomico, vicolo dell'Osservatorio, 5, I 35122, Padova, Italy

S. R. VARNAS: Department of Mathematics, Monash University, Clayton, Victoria 3168, Australia